2016

A High-Precision Near-Infrared Survey for Radial Velocity Variable Low-Mass Stars using CSHELL and a Methane Gas Cell

Jonathan Gagne

Peter Plavchan
Missouri State University

Peter Gao

Guillem Anglada-Escude

Elise Furlan

See next page for additional authors

Recommended Citation

Gagné, Jonathan, Peter Plavchan, Peter Gao, Guillem Anglada-Escude, Elise Furlan, Cassy Davison, Angelle Tanner et al. "A high-precision near-infrared survey for radial velocity variable low-mass stars using CSHELL and a methane gas cell." The Astrophysical Journal 822, no. 1 (2016): 40.

The Astrophysical Journal, 822:40 (24pp), 2016 May 1 doi:10.3847/0004-637X/822/1/40

A HIGH-PRECISION NEAR-INFRARED SURVEY FOR RADIAL VELOCITY VARIABLE LOW-MASS STARS USING CSHELL AND A METHANE GAS CELL

Jonathan Gagné[1,22], Peter Plavchan[2], Peter Gao[3], Guillem Anglada-Escude[4,5], Elise Furlan[6], Cassy Davison[7], Angelle Tanner[8], Todd J. Henry[7], Adric R. Riedel[9], Carolyn Brinkworth[6,10], David Latham[13], Michael Bottom[14], Russel White[7], Sean Mills[11], Chas Beichman[12], John A. Johnson[13], David R. Ciardi[6], Kent Wallace[15], Bertrand Mennesson[15], Kaspar von Braun[16], Gautam Vasisht[15], Lisa Prato[16], Stephen R. Kane[17], Eric E. Mamajek[18], Bernie Walp[19], Timothy J. Crawford[15], Raphaël Rougeot[20], Claire S. Geneser[2], and Joseph Catanzarite[21]
[1] Carnegie Institution of Washington DTM, 5241 Broad Branch Road NW, Washington, DC 20015, USA; jgagne@carnegiescience.edu
[2] Department of Physics, Missouri State University, 901 S National Ave, Springfield, MO 65897, USA; peterplavchan@missouristate.edu
[3] Division of Geological and Planetary Sciences, California Institute of Technology, Pasadena, CA 91125, USA
[4] School of Physics and Astronomy, Queen Mary University of London, 327 Mile End Rd, E1 4NS, London, UK
[5] Centre for Astrophysics Research, University of Hertfordshire, College Lane, AL10 9AB, Hatfield, UK
[6] NASA Exoplanet Science Institute, California Institute of Technology, 770 S. Wilson Ave., Pasadena, CA 91125, USA
[7] Department of Physics and Astronomy, Georgia State University, Atlanta, GA 30303, USA
[8] Mississippi State University, Department of Physics & Astronomy, Hilbun Hall, Starkville, MS 39762, USA
[9] Division of Physics, Mathematics and Astronomy, California Institute of Technology, Pasadena, CA 91125, USA
[10] National Center for Atmospheric Research, P.O. Box 3000, Boulder, CO 80307, USA
[11] Department of Astronomy and Astrophysics, University of Chicago, 5640 S. Ellis Ave, Chicago, IL 60637, USA
[12] NASA Exoplanet Science Institute, California Institute of Technology, Pasadena, CA 91125, USA
[13] Institute for Theory and Computation, Harvard-Smithsonian Center for Astrophysics, 60 Garden St., Cambridge, MA 02138 USA
[14] Department of Astronomy, California Institute of Technology, Pasadena, CA 91125, USA
[15] Jet Propulsion Laboratory, California Institute of Technology, 4800 Oak Grove Dr, Pasadena, CA 91125, USA
[16] Lowell Observatory, West Mars Hill Road, Flagstaff, AZ 86001, USA
[17] Department of Physics & Astronomy, San Francisco State University, 1600 Holloway Ave, San Francisco, CA 94132, USA
[18] Department of Physics & Astronomy, University of Rochester, Rochester, NY 14627, USA
[19] Stratospheric Observatory for Infrared Astronomy, NASA Dryden Flight Research Center, Mail Stop DAOF, S233, P.O. Box 273 Edwards, CA 93523, USA
[20] ESA, European Space Research and Technology Centre, Keplerlaan 1, 2201 Noordwijk, The Netherlands
[21] NASA Ames Research Center, MS 245-3, P.O. Box 1, Moffett Field, CA 94035-0001, USA
Received 2015 November 15; accepted 2016 March 1; published 2016 May 3

ABSTRACT

We present the results of a precise near-infrared (NIR) radial velocity (RV) survey of 32 low-mass stars with spectral types K2–M4 using CSHELL at the NASA InfraRed Telescope Facility in the *K* band with an isotopologue methane gas cell to achieve wavelength calibration and a novel, iterative RV extraction method. We surveyed 14 members of young (≈25–150 Myr) moving groups, the young field star ε Eridani, and 18 nearby (<25 pc) low-mass stars and achieved typical single-measurement precisions of 8–15 m s^{-1}with a long-term stability of 15–50 m s^{-1} over longer baselines. We obtain the best NIR RV constraints to date on 27 targets in our sample, 19 of which were never followed by high-precision RV surveys. Our results indicate that very active stars can display long-term RV variations as low as ∼25–50 m s^{-1} at ≈2.3125 μm, thus constraining the effect of jitter at these wavelengths. We provide the first multiwavelength confirmation of GJ 876 bc and independently retrieve orbital parameters consistent with previous studies. We recovered RV variabilities for HD 160934 AB and GJ 725 AB that are consistent with their known binary orbits, and nine other targets are candidate RV variables with a statistical significance of 3σ–5σ. Our method, combined with the new iSHELL spectrograph, will yield long-term RV precisions of $\lesssim$5 m s^{-1} in the NIR, which will allow the detection of super-Earths near the habitable zone of mid-M dwarfs.

Key words: planetary systems – planets and satellites: detection – stars: low-mass – techniques: radial velocities

Supporting material: figure set, machine-readable tables

1. INTRODUCTION

The method of Doppler radial velocity (RV) variations has proven itself fruitful in the last decades both for the identification of new exoplanets (e.g., Mayor & Queloz 1995; Marcy et al. 1998, 2001; Delfosse et al. 1998a; Cochran et al. 2002; Endl et al. 2003; Butler et al. 2004; Rivera et al. 2005b, 2010; Meschiari et al. 2011; Dumusque et al. 2012; Montet et al. 2014; Tuomi et al. 2014) and for the confirmation of exoplanets detected by the method of transit (e.g., Kepler-78b; Akeson et al. 2013; Pepe et al. 2013; Sanchis-Ojeda et al. 2013). Recent developments have shown that cool ($\lesssim$3800 K) stellar hosts in the M spectral class represent valuable targets for the identification of new Earth-mass planetary companions in the habitable zone using the RV method due to their smaller mass and significantly larger population (Henry et al. 2006).

However, it becomes gradually harder to obtain sufficient signal-to-noise ratios (S/Ns) at optical wavelengths at decreasing effective temperatures (Reiners et al. 2010; Bottom et al. 2013). To worsen the case, late-type M dwarfs are on average more active and display more stellar spots (e.g., Shkolnik et al. 2009; Morin et al. 2010; Shkolnik et al. 2012; Malo et al. 2014; Schmidt et al. 2015), which can induce RV

[22] NASA Sagan Fellow.

signals very similar to those of planetary companions (e.g., Queloz et al. 2001; Paulson & Yelda 2005). Robertson et al. (2014) demonstrated the importance of a careful consideration of stellar activity in exoplanet searches by demonstrating that the purported GJ 581 d habitable-zone exoplanet (Udry et al. 2007) was most likely a false-positive signal caused by stellar spots. Overcoming this limitation is especially important in the search for very-low-mass companions that induce RV variations of low amplitudes (e.g., a few $m\,s^{-1}$) comparable to stellar activity jitter.

The study of RV variations in the regime of near-infrared (NIR) wavelengths addresses both these issues. First, a larger fraction of the flux of cooler ($\lesssim$3850 K), later-type ($\gtrsim$M0; Pecaut & Mamajek 2013) host stars is emitted at these wavelengths, although care must be used in choosing the observed NIR wavelength range for M0–M4 dwarfs as their lack of spectral features can counterbalance the brightness advantage (Reiners et al. 2010).

Second and perhaps more importantly, the RV signal induced by stellar spots is expected to have an $\approx\lambda^{-1}$ dependence for modest spot contrast temperatures, where λ is the wavelength (Reiners et al. 2010; Anglada-Escudé et al. 2012; Howard et al. 2013; Pepe et al. 2013; Marchwinski et al. 2015; Plavchan et al. 2015), which means that the effect of stellar spots on NIR RV measurements is less important than it is at visible wavelengths by a factor ∼4. However, there have also been predictions that the Zeeman effect resulting from the strong magnetic activity in young stars could cause jitter to increase as a function of wavelength (Reiners et al. 2013). Furthermore, the RV signal induced on a stellar host by a substellar companion via the Doppler effect is independent of wavelength, so a multiwavelength RV follow-up opens the possibility of rejecting exoplanet candidates that are caused by other astrophysical phenomena that would cause RV variations of different amplitudes in the optical and NIR regimes.

RV surveys in the NIR are still trailing behind their optical counterparts in terms of long-term RV stability, with the best reported NIR results at $\approx$5 $m\,s^{-1}$ (Bean et al. 2010) using 8 m–class telescopes, or $\approx$45–60 $m\,s^{-1}$ (Blake et al. 2010; Crockett et al. 2011; Bailey et al. 2012; Tanner et al. 2012; Trifonov et al. 2015) using smaller facilities, versus 0.8–15 $m\,s^{-1}$ in the optical (Cochran & Hatzes 1994; Kürster et al. 1994; Endl et al. 2006; Mayor & Udry 2008; Howard et al. 2010b; Dumusque et al. 2012). This is mainly due to the presence of stronger telluric absorption features in the NIR (Blake et al. 2010; Seifahrt et al. 2010; Blake & Shaw 2011; Plavchan et al. 2015) and technical challenges, given that NIR instrumentation and observing methods have only been developed relatively recently. As an example, iodine gas cells, which have been used extensively as wavelength calibrators in optical RV surveys, do not offer a sufficient density of absorption lines in the NIR domain. For this reason, most existing NIR RV studies have used telluric lines to achieve wavelength calibration (Blake et al. 2010; Crockett et al. 2011; Bailey et al. 2012; Tanner et al. 2012; Davison et al. 2015), with the exception of Bean et al. (2010), who used an ammonia gas cell with CRyogenic high-resolution InfraRed Echelle Spectrograph (CRIRES) at the VLT to obtain unprecedented long-term precisions of $\approx$5–10 $m\,s^{-1}$ in the NIR on targets with K_S-band magnitudes between 4.4 and 8.0.

Our team has recently developed a methane isotopologue gas cell that offers a high absorption line density in the NIR regime to achieve RV measurements of the order of a few $m\,s^{-1}$ with the limited spectral grasp of CSHELL at the NASA InfraRed Telescope Facility (IRTF; Anglada-Escudé et al. 2012; Plavchan et al. 2013), as well as an iterative algorithm that allows for the simultaneous solving of the wavelength solution, the construction of an empirical stellar spectrum, and the measurement of stellar RVs (P. Gao et al., submitted to PASP). In this paper, we present the results of an NIR RV survey of 32 late-type, nearby stars using CSHELL at the IRTF using this new RV extraction pipeline. We achieve long-term, single-measurement, high-S/N RV precisions of $\approx$8 $m\,s^{-1}$ within a single night and $\approx$15 $m\,s^{-1}$ over long-term baselines up to several years, which represents a substantial improvement over previously reported single-measurement precisions using CSHELL and no gas cell (e.g., 58 $m\,s^{-1}$ within a single night, Crockett et al. 2011; or 90 $m\,s^{-1}$ on baselines of several years, Davison et al. 2015).

In Section 2, we present the method by which we constructed our target sample. The observing setup and strategy are then detailed in Section 3. We summarize the spectral extraction method and the RV measurement algorithm in Sections 4 and 5, respectively. The method by which we combine individual RV measurements is presented in Section 6. Our global survey results are then presented in Section 7, and we discuss individual targets in Section 8. We finally present our conclusions in Section 9.

2. SAMPLE SELECTION

Our survey sample is composed of two parts: the first consists of nearby, young stars mostly selected from known members of young moving groups, and the second consists of nearby (<25 pc) stars of any age. Comparing our results with those of optical RV surveys for the young sample will eventually allow us to characterize how the signature of stellar activity on RV curves differs between these two wavelength regimes, whereas completing the census of giant close-in planets in a volume-limited sample will be useful for deriving population statistics in the near future. In this section, we describe the process by which these samples were constructed. The complete survey sample is presented in Table 1, and a spectral-types histogram of it is presented in Figure 1.

2.1. The Young Sample

The young sample was constructed by selecting K- to mid-M-type young stars in the solar neighborhood, mainly from known members of young moving groups, such as β Pictoris (24 ± 3 Myr; Zuckerman et al. 2001; Bell et al. 2015a), AB Doradus (149^{+51}_{-19} Myr; Zuckerman et al. 2004; Bell et al. 2015a), and the Octans-Near association (≈30–100 Myr; Zuckerman et al. 2013), with Two Micron All Sky Survey (2MASS) K_S-band magnitudes brighter than 7.1 (the brightest target, ε Eridani, has $K_S = 1.8$) so that an S/N of ∼80 could be achieved within approximately an hour. The young age of all stars in this sample is strongly constrained by kinematic membership in these young associations, typically in addition to lithium abundance measurements or comparison to isochrones (e.g., Torres et al. 2008), except for the star ε Eridani, which is not a member of any known young moving group. In this case, the age is constrained to 400–800 Myr by Mamajek & Hillenbrand (2008).

Table 1
Precise NIR RV Follow-up Sample

Common Name	R.A. J2000 (hh:mm:ss)	decl. J2000 (dd:mm:ss)	Sp. Type	Ref.	2MASS K_S	$v \sin i$ (km s^{-1})	Ref.	Binary Sep. ($''$)	Ref.	$\log R'_{HK}$	Activity[a]	Ref.
Nearby, Young Sample												
AT Mic B	20:41:51.147	−32:26:10.22	M4	27	4.94[b]	15.8 ± 1.2	12	3.6	⋯	⋯	⋯	⋯
AT Mic A	20:41:51.156	−32:26:06.58	M4	27	4.94[b]	10.1 ± 1.2	12	3.6	⋯	⋯	⋯	⋯
au Mic	20:45:09.492	−31:20:26.66	M1	27	4.53	9.3 ± 1.2	12	⋯	⋯	−4.053 ± 0.057	VA	11
EQ Peg A	23:31:52.087	19:56:14.22	M3.5	28	5.33	12.8 ± 5.0	10	5.0	14	(−5.162 ± 0.057)	(VI)	6
Young Sample												
AG Tri	02:27:29.254	30:58:24.61	K8	27	7.08	5 ± 2	1	22.2	2	⋯	⋯	⋯
ε Eridani	03:32:55.911	−09:27:29.86	K2	29	1.78	2.45 ± 0.5	3	⋯	⋯	−4.478 ± 0.031	A	4
V577 Per	03:33:13.491	46:15:26.53	K2	5	6.37	8.9 ± 0.9	38	⋯	⋯	−4.109 ± 0.057	VA	6
GJ 3305 AB	04:37:37.467	−02:29:28.45	M0	30	6.41	6.50 ± 0.5	7	0.093	⋯	⋯	⋯	⋯
TYC 5899–26–1	04:52:24.407	−16:49:21.97	M3	27	6.89	<3	5	⋯	⋯	⋯	⋯	⋯
V1005 Ori	04:59:34.831	01:47:00.68	M0	27	6.26	8.7 ± 0.9	8	⋯	⋯	−4.080 ± 0.151	VA	8
BD+20 1790	07:23:43.592	20:24:58.66	K5	31	6.88	15.70 ± 3.16	9	⋯	⋯	−3.800 ± 0.0037	VA	8
BD+01 2447	10:28:55.551	00:50:27.62	M2	27	5.31	0.1 ± 0.2	10	⋯	⋯	−5.029 ± 0.057	I	11
HD 160934 AB	17:38:39.634	61:14:16.03	M0	27	6.81	19.1 ± 0.6	8	0.12	⋯	−3.87 ± 0.120	VA	8
LO Peg	21:31:01.711	23:20:07.47	K8	27	6.38	70 ± 10	10	⋯	⋯	−3.906 ± 0.050	VA	13
BD–13 6424	23:32:30.864	−12:15:51.43	M0	27	6.57	8.8 ± 1.2	12	⋯	⋯	⋯	⋯	⋯
Nearby Sample												
GJ 15 A	00:18:22.885	44:01:22.63	M2	32	4.02	1.43 ± 0.5	7	31.9	2	−5.27 ± 0.04	VI	8
GJ 169	04:29:00.138	21:55:21.48	M0.5	33	4.88	3.8 ± 1.8	10	⋯	⋯	−4.813 ± 0.154	I	8
LHS 26	04:31:11.479	58:58:37.57	M4	32	5.72	<3	15	8.9	2	⋯	⋯	⋯
GJ 338 A	09:14:22.982	52:41:12.53	M0	32	3.99	2.9 ± 1.2	16	18.1	17	−4.652 ± 0.166	A	8
GJ 338 B	09:14:24.856	52:41:11.84	M0	32	4.14	2.8 ± 1.2	16	18.1	17	−4.420 ± 0.050	A	18
GJ 458 A	12:12:20.847	54:29:08.69	M0	31	6.06	5.4 ± 1	8	14.7	20	−4.970 ± 0.040	I	8
GJ 537 B	14:02:33.128	46:20:23.92	M0	34	5.39	<4	21	3.0	⋯	(−4.971 ± 0.057)	(I)	4
GJ 537 A	14:02:33.240	46:20:26.64	M2	34	5.43	<4	21	3.0	2	−4.733 ± 0.057	A	4
LHS 371	14:25:43.496	23:37:01.06	M0	34	5.97	<4	21	45.4	20	⋯	⋯	⋯
LHS 372	14:25:46.671	23:37:13.31	M1	34	6.09	<4	21	45.3	22	⋯	⋯	⋯
LHS 374	14:30:47.794	−08:38:46.57	M0	34	5.77	<3	10	50.0	23	−4.896 ± 0.057	I	24
GJ 9520	15:21:52.919	20:58:39.48	M1.5	31	5.76	6.5 ± 3	21	⋯	⋯	⋯	⋯	⋯
GJ 3942	16:09:03.097	52:56:37.95	M0	35	6.33	<4	21	⋯	⋯	⋯	⋯	⋯
GJ 725 A	18:42:46.679	59:37:49.47	M3	32	4.43	<2.5	26	13.3	⋯	−5.267 ± 0.229	VI	11
GJ 740	18:58:00.140	05:54:29.70	M0.5	21	5.36	3.8 ± 2.8	8	⋯	⋯	−4.825 ± 0.175	I	8
EV Lac	22:46:49.807	44:20:03.10	M3.5	36	5.30	6.9 ± 0.8	8	10.0	2	−3.972 ± 0.147	VA	8
GJ 876	22:53:16.722	−14:15:48.91	M4	37	5.01	2.8 ± 2.2	25	⋯	⋯	(−5.146 ± 0.057)	(VI)	11

Notes. See Section 2 for more details.
[a] VI: Very inactive; I: Inactive; A: Active; VA: Very active; ⋯: Information not available in the literature (see Section 2.2 for more details).
[b] Unresolved photometry.

References. (1) Cutispoto et al. (2000), (2) Mason et al. (2001), (3) Butler et al. (2006), (4) Duncan et al. (1991), (5) Schlieder et al. (2010), (6) Pace (2013), (7) Houdebine (2010), (8) Herrero et al. (2012), (9) White et al. (2007), (10) Głębocki & Gnaciński (2005), (11) Isaacson & Fischer (2010), (12) Torres et al. (2006), (13) Gray et al. (2003), (14) Fabricius et al. (2002), (15) Mohanty & Basri (2003), (16) Delfosse et al. (1998b), (17) Orlov et al. (2012), (18) Eiroa et al. (2013), (19) Stelzer et al. (2013), (20) Lépine & Bongiorno (2007), (21) Reiners et al. (2012), (22) Salim & Gould (2003), (23) Worley & Douglass (1997), (24) Arriagada (2011), (25) Marcy & Chen (1992), (26) Browning et al. (2010), (27) Malo et al. (2013), (28) Davison et al. (2015), (29) Keenan & McNeil (1989), (30) Kasper et al. (2007), (31) Reid et al. (2004), (32) Jenkins et al. (2009), (33) Koen et al. (2010), (34) Gaidos et al. (2014), (35) Vyssotsky (1956), (36) Hawley et al. (1997), (37) Lafrenière et al. (2007), (38) McCarthy & Wilhelm (2014).
(This table is available in machine-readable form.)

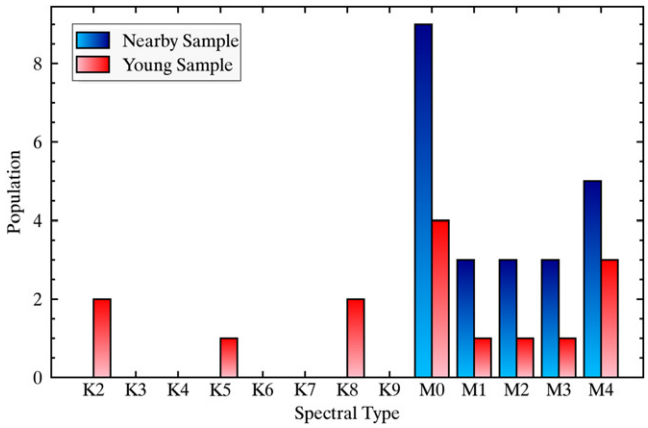

Figure 1. Spectral-type histogram of the nearby and young target samples that were studied in this work. Targets that fall into both samples are shown in both histograms (and thus appear twice). For more details, see Section 2.

No selection cut was applied on projected rotational velocities; all stars in this sample have measured $v \sin i$ values in the literature ranging from 2 to 70 km s^{-1}. All $<2''$ binaries were rejected from the sample, except for GJ 3305 AB ($0\farcs093$; Kasper et al. 2007) and HD 160934 AB ($0\farcs12$; Gálvez et al. 2006), which were not known to be binary stars at the time when the young sample was assembled. A total of 15 targets were selected and are listed in Table 1, with spectral types ranging from K2 to M4.

Six targets in the young sample had never benefited from a precise RV follow-up. Six others were already followed either at optical or NIR wavelengths, albeit at a $\gtrsim$50 m s^{-1} precision (AG Tri, AT Mic A, AT Mic B, au Mic, BD+01 2447, V1005 Ori; Paulson & Yelda 2006; Bailey et al. 2012), and three targets benefited from a precise RV follow-up at optical wavelengths (BD+20 1790,ε Eridani, GJ 3305 AB; e.g., Campbell et al. 1988; Figueira et al. 2010; Elliott et al. 2014; Hernán-Obispo et al. 2015).

There are a total of three out of 15 (20%) targets in the young sample that have a projected rotational velocity smaller than ~3 km s^{-1}, which seems unexpected for young stars (i.e., such slow rotators have been shown to be typically older than a few hundred Myr; Irwin et al. 2011; Reiners & Mohanty 2012). We suggest that projection effects could explain this; for example, 20% of stars with a random inclination i would have projected rotational velocities three times smaller or less than their actual rotational velocities (i.e., $\sin i \leqslant 0.31$).

2.2. The Nearby Sample

The nearby sample was constructed by selecting all M dwarfs from the Research Consortium on Nearby Stars (Henry et al. 2014) and the Lépine and Shara Proper Motion catalog (Lépine 2005) with a trigonometric distance measurement that places them within 25 pc of the Sun. We avoided including targets that were already part of precise RV follow-up programs, such as the Hobble-Eberly Telescope survey (HET; Endl et al. 2003, 2006), the California Planet Survey (CPS; Howard et al. 2010a; Montet et al. 2014), and the Ultraviolet and Visual Echelle Spectrograph reanalysis of Tuomi et al. (2014). We selected the targets that are easily accessible from the IRTF ($-35° <$ Decl. $< 65°$) with apparent 2MASS magnitudes of $K_S < 6.4$. We used a more conservative K_S-band cut in this sample to achieve an S/N of at least 200 per pixel within a few hours (see Section 3).

All targets with a known stellar companion or a background star at $<2''$ were rejected from the sample. We obtained projected rotational velocities ($v \sin i$) from the literature when available and rejected targets with $v \sin i \geqslant 20$ km s^{-1}. From this initial list of targets, we followed 21 low-mass stars with spectral types in the M0–M4 range, which are listed in Table 1. All of these targets have rotational velocity measurements in the literature, which range from 3 to 16 km s^{-1}. It can be noted that four targets are present in both the nearby and young samples.

Fourteen targets in the nearby sample never had precise RV follow-up observations. Five targets were already followed at NIR wavelengths, albeit at a $\gtrsim$50 m s^{-1} precision (AT Mic A, AT Mic B, au Mic, EV Lac, and GJ 725 A; Bailey et al. 2012), and two other targets benefited from a precise RV follow-up at optical wavelengths (GJ 15 A and GJ 876; e.g., Delfosse et al. 1998a; Marcy et al. 1998; Rivera et al. 2010; Howard et al. 2014).

Both the HET and CPS catalogs used similar selection criteria, with the exception that young or chromospherically active systems were rejected. Thus, we are subject to a bias toward these systems despite our rejection of high–$v \sin i$ targets. One target in the sample (GJ 740) has been followed as part of the HARPS survey (Bonfils et al. 2013), but no results were published at the time the target list was assembled, so we have included it in the sample.

We flag chromospheric activity in Table 1 based on $\log R'_{HK}$ index values from the literature, when available (e.g., see Zirker 1968; Noyes et al. 1984). We assume a measurement error of 5% in the case of LO Peg since Gray et al. (2003) do not report one. Nine objects have no available $\log R'_{HK}$ index but have a measurement for the alternative S_{HK} index that also traces chromospheric activity. In these cases, we used the relation of Middelkoop (1982) and Noyes et al. (1984) to translate it into a value for $\log R'_{HK}$. Using Figure 1 of Middelkoop (1982),[23] we calculated that this relation is associated with an uncertainty of ~0.057 dex, which is larger than the typical measurement errors on S_{HK} themselves. In a few cases where the $B - V$ color of a target is redder than the color range where the relation has been tested ($0.45 \leqslant B - V \leqslant 1.5$), we display the value between parentheses in Table 1. We use the classification of Gray et al. (2003) to categorize targets with $\log R'_{HK} > -4.2$ as very active (VA), those with $-4.2 > \log R'_{HK} > -4.75$ as active (A), those with $-4.75 > \log R'_{HK} > -5.1$ as inactive (I), and those with $\log R'_{HK} < -5.1$ as very inactive (VI).

3. OBSERVATIONS

We obtained our data using the NIR high-resolution single-order echelle spectrograph CSHELL (Tokunaga et al. 1990; Greene et al. 1993) at the 3 m IRTF from 2010 October to 2015 January. The survey presented here includes a total of 3794 individual spectra obtained within a total of 65 observing nights. We used the $0\farcs5$ slit and the continuous variable filter,[24] yielding a resolving power of $R = 46{,}000$ (Crockett

[23] Using the WebPlotDigitizer tool available at http://arohatgi.info/WebPlotDigitizer/.

[24] More information is available at http://irtfweb.ifa.hawaii.edu/~cshell/rpt_cvf.html.

Table 2
Log of All Science Star Observations

Target Name	UT Date (YYMMDD)	Num. of Spectra	Median S/N
AG Tri	101009	6	23
	101011	15	16
	101012	12	23
	101122	12	22
	101123	12	26
	101124	12	20
	110216	9	22
	110219	10	25
	110716	10	20
	110819	14	28
AT Mic A	101010	6	39
	101011	11	35
	101013	10	28
	101123	2	26
	101124	6	43

Note. See Section 3 for more details.

(This table is available in its entirety in machine-readable form.)

et al. 2011; Prato et al. 2015) with a spectral grasp of ≈5.55 nm at 2.3125 μm. It is noteworthy to mention that Davison et al. (2015) measured a resolving power as high as $R = 57{,}000$ with the 0.″5 slit from modeling observed absorption telluric lines and suggested that this could be due to the slit being slightly narrower than its designation. The spectrograph uses a ≈25 year old 256 × 256 pixel InSb detector that has a significant number of bad pixels compared to more recent NIR detectors.

A $^{13}CH_4$ isotopologue methane gas cell (Anglada-Escudé et al. 2012; Plavchan et al. 2013) was inserted in the shutter beam to provide a wavelength reference in the NIR. The gas cell temperature was stabilized at 10.°0 ± 0.°1 Celsius, which is adequate to keep it stable at better than the ∼1 m s^{-1} level (Anglada-Escudé et al. 2012; Plavchan et al. 2013). The grating angle was set once at the beginning of each night by observing an A-type star and ensuring that the deep methane absorption line of the gas cell at ≈2.31355 μm was located on column 179 of the detector to achieve identical wavelength coverage, as the position of the deep methane feature typically varied by ∼1–2 detector pixels between observing nights. This setup typically corresponded to central wavelength values of ≈2.31255 μm.

We obtained science exposures of 300 s or less to avoid saturation or significant background variations, and we obtained several exposures (typically ∼5–60) to achieve a combined S/N of ∼70–200 depending on the survey sample. We did not obtain pair-subtracted spectra as our targets are significantly brighter than background sky emission, and all spectra were obtained with the methane gas cell in the beam.

Starting in 2014, we systematically observed one bright A-type star (either Sirius, Castor, Vega, Alphecca, β Arietis, or 32 Pegasi, depending on their altitude) at the beginning of every night to obtain an S/N ≈ 200 spectrum of the gas cell and to characterize any potential long-term variation. Fifteen flat-field exposures of 15 s were initially obtained at the beginning of every night, but starting from 2014 April 2, we obtained fifteen 15 s flat-field exposures after every science target to minimize systematic instrumental effects. We did not apply dark-frame calibrations because we found that they did not improve the quality of our results. A log of all observations obtained in this work is presented in Table 2, where S/N values are calculated by assuming that the spectra are photon-noise limited.

4. SPECTRAL EXTRACTION

Because of several challenges in extracting RVs out of CSHELL spectra, we constructed our own custom data-reduction pipeline to extract the 3794 spectra obtained in this work in a consistent way. We summarize below this data-extraction pipeline, which is described in more detail in Gao et al. (2016).

Per-target flat fields were generated by median-combining data sets that each consist of 15 individual files. Two-dimensional (2D) sinusoidal fringing with amplitude ∼0.2%–0.6% was found to be present in these flat fields and was due to the CSHELL circular variable filter, which limited our long-term RV precision to >55 m s^{-1} when left uncorrected. Fringing subtraction was thus achieved by median-combining a large number of per-target flat fields spanning several years to obtain a master flat field. This averaged out the fringing that was due to its spatial and spectral variations over time. Individual per-target flat fields were then normalized by the master flat field to bring out their fringing pattern, which was fitted and corrected individually.

Fringing is also present in the science observations, but similar efforts to correct fringing were not possible because of the low illumination of most of the image aside from the spectral trace of the target. Thus, we removed this fringing in the RV extraction process.

Spectral extraction was performed by first dividing the fringing-corrected, per-target flat fields from the science observations, followed by correcting for a linear tilt in the target trace on the detector. A Moffat profile was then fit to the trace in the spatial direction, and the 1D spectrum was extracted using the median trace profile with an optimal extraction procedure (Horne 1986; Massey & Hanson 2013). Following this, a synthetic spectral trace was constructed from the extracted spectrum and the spatial profile and was divided out from the observed spectral trace. The 2D residuals resulting from this operation were combed for large deviations from the median, which were flagged as bad pixels. A 1D spectrum was extracted again from the spectral trace after masking these bad pixels. Additional bad pixels were flagged by noting any major deviations from the continuum in the final 1D spectra, in order for them to be ignored by the RV extraction pipeline.

5. RADIAL VELOCITY EXTRACTION

We used a novel forward-modeling MATLAB RV pipeline to compute the relative RV of every individual spectrum, which we summarize in this section. The pipeline is described in detail by P. Gao et al. (submitted to PASP), who demonstrate that it allows for the construction of a stellar template simultaneous with gas cell observations and properly accounts for the significant telluric features in the NIR. Using this pipeline with CSHELL/IRTF data, they achieve an RV precision of ∼3 m s^{-1} over a few days using photon-noise-limited observations of the M-type giant SV Peg.

The pipeline extracts the RVs associated with a spectrum by fitting a forward spectral model to the observed data. The forward model consists of an empirical telluric transmission

spectrum T_λ (Livingston & Wallace 1991), where λ is the wavelength measured at rest and in vacuum; a measured isotopologue methane gas cell spectrum G_λ (Plavchan et al. 2013) that was obtained from the NASA Jet Propulsion Laboratory (JPL) and is corrected using high-S/N observations of A-type telluric standards; a line-spread function (LSF) L that models broadening and distortions in the spectral line profile due to both instrumental and atmospheric effects and that is represented by a weighted sum of the first five terms of the Hermite function (i.e., a normal distribution multiplied by Hermite polynomials; see Arfken et al. 2012) where the weights are free parameters; a quadratic curve B_λ that models the instrumental blaze function and variations in the NIR sky background; and an instrumental fringing term ϕ_λ that is represented by a multiplicative sinusoid function. The forward model F_λ is then given by

$$F_\lambda = (G_\lambda \cdot T_\lambda \cdot S_\lambda \cdot B_\lambda \cdot \phi_\lambda) \otimes L, \quad (1)$$

where S_λ is an estimated stellar spectrum of the target in the absence of a gas cell, and $\otimes$ represents a convolution. The forward model F_λ must then be Doppler shifted to account for the relative line-of-sight velocity of the target with respect to an observer on Earth. This is done by applying a linear shift to F_λ by a factor (W/c) in logarithmic wavelength space, where c is the speed of light and W is the combined contributions from the RV signal of the target and the motion of the Earth relative to the target. Finally, F_λ is mapped to the detector pixels using a two-degree polynomial mapping relation. The forward model is fit to the data using a Nelder–Mead downhill simplex algorithm (Nelder & Mead 1965), which is especially useful in this situation where the number of free parameters (17) is relatively large.

A difficulty in using this method is the apparent need to measure the stellar spectrum S_λ, which would require obtaining high-S/N spectra for every target with the methane gas cell out of beam. This would be problematic because moving the methane gas cell in and out of beam will affect the wavelength solution of the observed spectrum. The stellar template thus needs to be measured simultaneously with the collection of the RV data. The algorithm addresses this need, using only observations obtained with the gas cell in the beam, by (1) performing a first fit with $S_\lambda = 1 \ \forall \lambda$; (2) identifying deep CO lines in the residuals of the best fit; (3) repeating step 1 with the CO lines masked to obtain a better solution given that CO lines are not yet included in the stellar template S_λ; (4) constructing a stellar spectrum from a weighted linear combination of the deconvolved fitting residuals of all individual spectra for a given science target in the stellar rest frame; and (5) repeating step 4 up to 20 times, adding the residuals back into the best estimated stellar spectrum at every iteration. The deconvolution of the residuals is computer intensive and only significantly benefits the first iteration, so it was only performed at the first iteration. It is important to note that all RVs measured with this algorithm are *relative* since they are measured with respect to the stellar template that was constructed from all of the data themselves.

It can be noted that combining all observations to create the stellar template does not account for any variability of the star within the wavelength range that we observe. This is not problematic for the targets in our sample since they do not show significant temporal variations in their spectral morphology, but stars that vary significantly, such as SV Peg (e.g., M. Bottom et al. 2016, in preparation), would need to be reduced in several individual steps of smaller temporal coverage to account for the varying stellar spectrum.

The quality of the fit typically increased for a few iterations (typically $\lesssim$10), until noise started to dominate the residuals that are added to the stellar spectrum. The best-fit parameters of the iteration where the RV scatter is minimized were then preserved as the true solution to the fit, and the barycentric-corrected RVs were calculated from W using barycentric corrections that were computed a priori for every science exposure with the *barycentric_vel.pro* IDL routine. Since the stellar spectrum is not modeled, this analysis does not allow for a measurement of the projected stellar rotational velocity.

6. THE COMBINATION OF RV MEASUREMENTS

The algorithm described in Section 5 yields an individual RV measurement ν_i for every spectrum i that corresponds to a single exposure on a given science target. These RV measurements are relative in the sense that they are computed with respect to the stellar template, which is built from the data themselves. The Nelder–Mead downhill simplex algorithm does not provide error measurements on the best-fit parameters, but the general quality of the forward model can be assessed from σ_{R_i}, the standard deviation of the residuals (R_i) of the best fit to the spectrum in question, with bad pixels ignored.

Since we aim to reach high S/Ns and to detect variability on timescales of more than several hours, we combined all science exposures obtained within a given night (typically ~5–60), using a weighted mean that is designed to minimize the impact of low-quality data:

$$\bar{\nu}_k = \frac{\sum_i w_i \, \nu_i}{\sum_i w_i}, \quad (2)$$

where the weight factors are defined as $w_i = \sigma_{R_i}^{-2}$. Thus $\bar{\nu}_k$ represents the mean RV within observing night k. We define the measurement error that is associated with this quantity as a weighted standard deviation of the individual RV measurements obtained in this night:

$$\sigma_k^2 = \frac{1}{N_{\rm exp}} \frac{\sum_i w_i \, (\nu_i - \bar{\nu}_k)^2}{\sum_i w_i}, \quad (3)$$

where $N_{\rm exp}$ is the total number of exposures obtained within the observing night.

There are a few quantities that are interesting to calculate for every RV curve, in the sense that they can shed light on the typical precision and on the possibility that a target is an RV variable source. The most straightforward of those is the weighted standard deviation of the per-night RVs:

$$\varsigma^2 = \frac{\sum_k w'_k \, \bar{\nu}_k^2}{\sum_k w'_k}, \quad (4)$$

where we use the ς symbol to distinguish this quantity from σ_k. We use the optimal weight factors w'_k that correspond to the inverse of the variance of a per-night RV measurement:

$$w'_k = \sigma_k^{-2}. \quad (5)$$

In order to avoid an artificial overweighting of RV points that have a very small σ_k, which happens from time to time

when the number of exposures is very low, we define a maximum weight of $w'_{k,\max} = (15\,\mathrm{m\,s^{-1}})^{-2}$, which corresponds to the weight that one RV data point would have at the typical single-measurement precision values that we obtain for high-S/N observations.

Another quantity of interest is the reduced chi-square χ^2_r of an RV curve with respect to a zero-variation curve, given by

$$\chi^2_r = \frac{1}{N_k - 1}\sum_{k=1}^{N_k}\frac{\bar{\nu}_k^2}{\sigma_k^2} \quad (6)$$

where N_k is the number of nights where a given target was observed, and the denominator $N_k - 1$ corresponds to the number of degrees of freedom to the RV curve (we subtract one fitted parameter corresponding to the floating relative RV). Targets with a higher χ^2_r value will be more likely to be true RV-variable sources.

In an ideal case where all per-night RV measurements have the same intrinsic RV precision $\sigma_k = S\ \forall k$, it can be shown from the previous equations that

$$S^2 = \frac{\varsigma^2}{\chi^2_r}\left(\frac{N_k}{N_k - 1}\right). \quad (7)$$

We will refer to this quantity S as the single-measurement precision; it is not affected by the fact that a given source is an RV variable as long as it is only variable on timescales longer than a few hours (otherwise σ_k would be partly composed of a variability term). For the sake of being able to compare all of our targets in a single ς^2–χ^2_r plane, we will make the following approximation:

$$S^2 \approx \frac{\varsigma^2}{\chi^2_r}, \quad (8)$$

which would normally only be valid for large values of N_k. We can bring out another interesting measurement by making the supposition that the scatter ς of a given RV curve is due to only two uncorrelated sources: a physical RV variability V and an instrumental error term corresponding to the single-measurement precision S. It immediately follows that

$$\varsigma = \sqrt{S^2 + V^2}. \quad (9)$$

We define another quantity N_ς:

$$N_\varsigma = \frac{V}{S} = \sqrt{(\varsigma/S)^2 - 1} \approx \sqrt{\chi^2_r - 1}, \quad (10)$$

which will be used in the following sections to assess the statistical significance of the RV variability V of our targets.

One last quantity of interest is $V_{\max}$, the maximal admissible RV variability on the timescales that we probed given our RV measurements, at a statistical significance ofN_ς. If we assume that the probability density function $\mathcal{N}(\nu)$ associated with the RV variability measurement that we obtained for a target is a normal distribution centered on V with a characteristic width S, a simplistic estimate for the maximal admissible RV variability would be $V_{\max} = V + N_\varsigma S$ such that

$$f = \int_{-\infty}^{V_{\max}(N_\varsigma)} \mathcal{N}(\nu)\,d\nu = \mathrm{erf}\,(N_\varsigma/\sqrt{2}) \approx 0.9973, \quad (11)$$

where $\mathrm{erf}\,(x)$ is the error function. However, since negative RV variabilities are unphysical, the normal probability density function must be set to zero for all negative RV values. We must thus identify the value for $V_{\max}$ that ensures

$$\int_0^{V_{\max}(N_\varsigma)} \mathcal{N}(\nu)\,d\nu = f\int_0^{\infty} \mathcal{N}(\nu)\,d\nu. \quad (12)$$

Solving for $V_{\max}$ yields

$$V_{\max}(N_\varsigma) = V + S\,\mathrm{erf}^{-1}(f - (1-f)\,\mathrm{erf}\,(V/S)), \quad (13)$$

$$f = \mathrm{erf}\,(N_\varsigma/\sqrt{2}), \quad (14)$$

where $\mathrm{erf}^{-1}(x)$ is the inverse error function.

Table 3
Detailed Radial Velocity Measurements

Target Name	Red. Julian Date JD-2400000	Relative RV ($\mathrm{m\,s^{-1}}$)	S/N Ratio
AG Tri	55479.003±0.003	107 ± 51	23
	55480.930±0.004	−139 ± 50	16
	55482.015±0.006	10 ± 27	23
	55522.875±0.003	198 ± 43	22
	55523.855±0.003	76 ± 45	26
	55524.871±0.003	−76 ± 77	20
	55608.734±0.004	64 ± 103	22
	55611.739±0.003	29 ± 50	25
	55759.126±0.004	26 ± 48	20
	55793.018±0.004	−77 ± 22	28
AT Mic A	55479.735±0.001	34 ± 25	39
	55480.729±0.004	0 ± 40	35
	55482.776±0.001	−15 ± 59	28
	55523.713±0.001	−97 ± 118	26

Note. See Section 7 for more details.

(This table is available in its entirety in machine-readable form.)

7. SURVEY RESULTS

We present in this section the NIR RV measurements that we obtained for the two survey samples described in Section 2 using our novel RV extraction method. The global results of this survey are described in Section 7.1, and upper limits on the projected masses of possible companions to our targets are derived in Section 7.2. We discuss the effect of rotational velocity and stellar activity in Section 7.3, and we discuss bisector measurements in Section 7.4.

7.1. Ensemble Results

The 248 individual per-night RV measurements ($\bar{\nu}_k$, σ_k) and epochs that were accumulated in this survey are listed in Table 3, and the associated RV curves are presented in Figures 2, 3, 4, and 5. The dominant cause of the variation in error bars for the per-night RVs presented in these figures is the varying S/Ns most often associated with weather or a varying number of total spectra.

We achieved short-term RV precisions (within a single night) as low as ∼8–15 $\mathrm{m\,s^{-1}}$ for higher-S/N observations, which represents a net improvement over previous studies that used similar small facilities (e.g., ≈45–90 $\mathrm{m\,s^{-1}}$; Bailey et al. 2012; Davison et al. 2015) but that did not benefit from a methane gas cell or our novel RV extraction method. These precisions are almost comparable to what is achieved using 8 m–class telescopes with a spectral grasp ∼10 times larger, although we can only achieve similar S/Ns on brighter targets

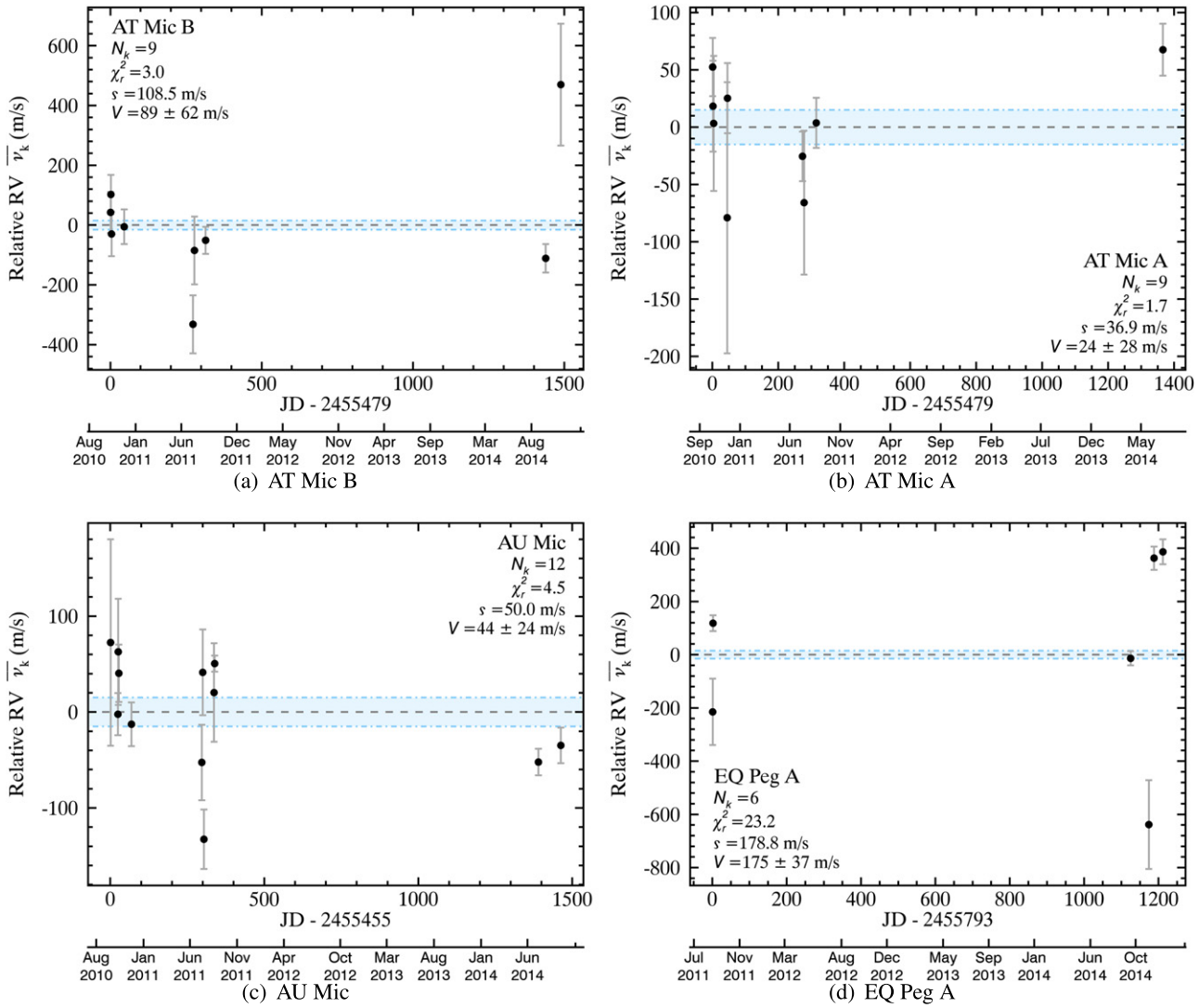

Figure 2. RV curves of the targets that are present in both the young and nearby samples. The gray dashed line corresponds to the relative zero level, whereas the light blue region delimited by dash-dotted lines corresponds to a scatter of 15 m s^{-1}, which is similar to the best average single-measurement precisions that we achieve. Target names are displayed in the legends, as well as the total number of measurements N_k, the error-weighted reduced chi-square χ_r^2 with respect to a zero-variation curve, the error-weighted standard deviation ς, and the expected RV variability V (see Section 6 for details). See Section 7 for a discussion of the global survey results and Section 8 for a discussion of individual targets.

(e.g., 5–10 m s^{-1} on targets with $4.4 < K_S < 8.0$; Bean et al. 2010).

In Table 4, we present the distributions of ς, χ_r^2, V, S, $V_{\max}(N_\varsigma = 1)$, and $V_{\max}(N_\varsigma = 3)$ for the two survey samples. The methane gas cell and RV extraction method that we used allowed us to achieve long-term RV precisions of $S \sim$ 15–50 m s^{-1}, which represents an improvement of a factor $\gtrsim$2 over similar NIR surveys that use small observing facilities. It can be noted that we obtain χ_r^2 values above 1 for the majority of targets in our survey. This is expected because the instrumental stability of CSHELL introduces a systematic RV uncertainty on the combined RV measurements $\bar{v}_k$ that is not captured by their error barsσ_k, which are determined from the weighted standard deviation of single-exposure RV measurements within one night (see Section 6). As a result, a χ_r^2 value above 1 alone does not imply that a given target is an RV variable. Hence, the survey targets must be compared relative to one another in order to determine which ones are most likely RV variables. It should also be noted that our survey is expected to have a larger number of RV variables than a blind survey because ours is biased toward young and active stars (see Section 2).

In Figures 6 and 7, we present the distributions of χ_r^2 and ς as a function of the total number of epochs for all of our targets. These figures bring out the absence of a correlation between these quantities, an indication that no significant long-term systematics are affecting our survey results.

In Figure 8, we present the reduced χ_r^2 with respect to zero RV variation as a function of the RV scatter ς for all of our targets. This figure illustrates how the young survey sample has been observed with a typically lower S/N, resulting in typical single-measurement precisions around 50 m s^{-1} on average, whereas those of the nearby sample are lower at around 15 m s^{-1}. Targets located in the upper right of the figure (along lines of constant single-measurement precisions) are the most secure RV variables.

A Kolmogorov–Smirnov test yields a 54% probability that the reduced χ_r^2 values around zero RV variation for the young and nearby samples are drawn from a single random distribution (the nearby sample targets have slightly larger χ_r^2

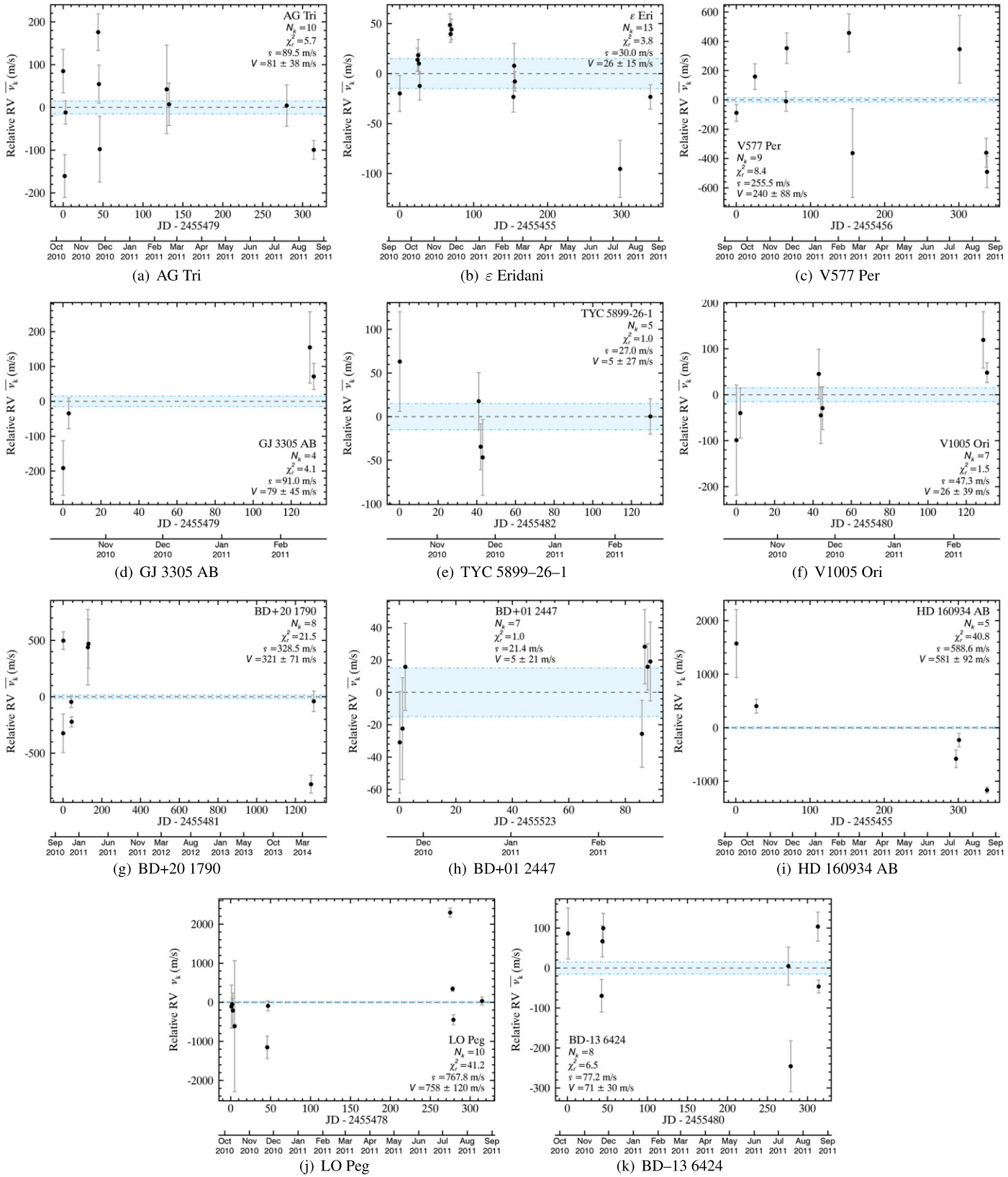

(a) AG Tri (b) ε Eridani (c) V577 Per

(d) GJ 3305 AB (e) TYC 5899–26–1 (f) V1005 Ori

(g) BD+20 1790 (h) BD+01 2447 (i) HD 160934 AB

(j) LO Peg (k) BD–13 6424

Figure 3. RV curves of the young target sample. The formatting is identical to that of Figure 2. See Section 7 for a discussion of the global survey results and Section 8 for a discussion of individual targets.

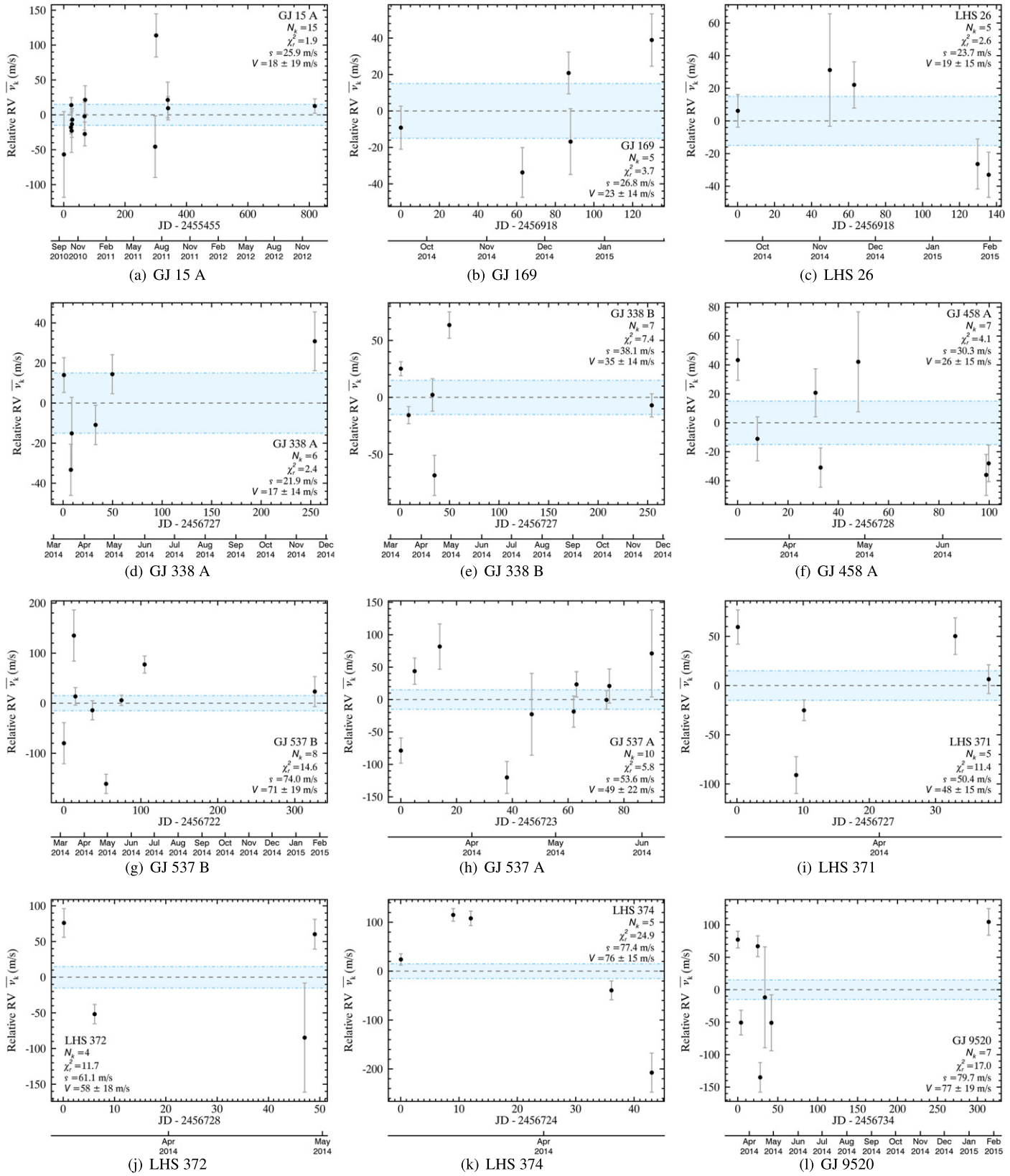

(a) GJ 15 A (b) GJ 169 (c) LHS 26

(d) GJ 338 A (e) GJ 338 B (f) GJ 458 A

(g) GJ 537 B (h) GJ 537 A (i) LHS 371

(j) LHS 372 (k) LHS 374 (l) GJ 9520

Figure 4. RV curves of the nearby target sample, part 1 of 2. The formatting is identical to that of Figure 2. See Section 7 for a discussion of the global survey results and Section 8 for a discussion of individual targets.

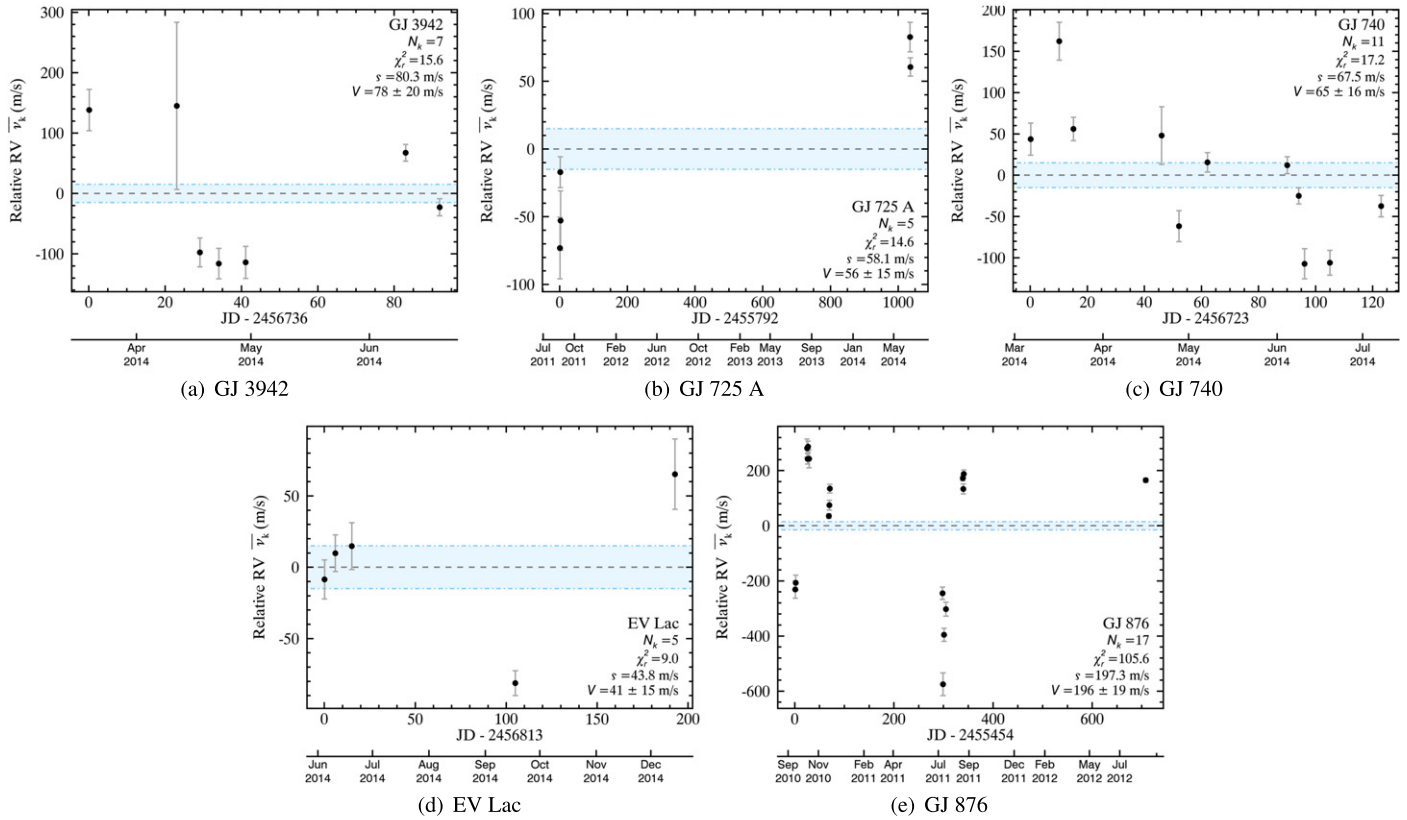

(a) GJ 3942 (b) GJ 725 A (c) GJ 740

(d) EV Lac (e) GJ 876

Figure 5. RV curves of the nearby target sample, part 2 of 2. The formatting is identical to that of Figure 2. See Section 7 for a discussion of the global survey results and Section 8 for a discussion of individual targets.

values on average). This indicates a weak statistical significance that there is any fundamental difference in the RV variability amplitude between the two samples. We recover a larger fraction of candidate RV-variable targets in the nearby sample ($10/21 \approx 48\%$) than in the young sample ($4/15 \approx 27\%$). However, considering Poisson statistics and the number of targets in each sample, there is a relatively large $\approx$23% chance that this discrepancy is due to pure chance. Both these results could be explained by the fact that we obtained higher-S/N observations on average for the nearby sample, if we assume that there is a larger number of RV variables with an amplitude small enough that they would not be detected in the young sample (see Figure 8).

In Figure 9, we show the RV variability V as a function of the single-measurement precision S and the statistical significance N_ς of V. The first distribution outlines the vastly different single-measurement precisions that were obtained for the young and nearby samples, which is an effect of the different S/N observations. Targets located higher up in panel (b) of Figure 9 are the most probable RV variables, and those located farther to the right in the same figure could correspond to more massive or close-in companions.

Nineteen of the targets presented in this work were never part of a precise RV follow-up ($S \lesssim 100\,\mathrm{m\,s^{-1}}$) to date. There are, however, 13 targets that already benefited from precise RV monitoring. These targets are listed in Table 5, where we compare the number of epochs, single-measurement precision, and RV scatter of existing optical and NIR surveys to our survey results. For eight of the targets listed in this table, we present a more precise RV follow-up to those already published, and for five of the targets, we present the first precise RV follow-up in the NIR. There is only one case (AT Mic B) for which an NIR follow-up already existed at a better precision than the results presented here. These data do not allow us to perform a significant comparison between the level of RV variability of single stars in the optical versus NIR; only three such targets (BD+01 2447, GJ 15 A, and ε Eridani) have precise RV measurements in both regimes, but they are consistent within 1σ.

7.2. Constraints from Nondetections

The upper-limit measurements on RV variability V_{max} defined in Equation (13) and listed in Table 4 can be translated to upper limits on companion masses as a function of physical separation or orbital period.

In order to estimate these upper limits, we have carried out a 10^8-step Monte Carlo simulation, where the orbital parameters of synthetic companions (projected companion mass $M_p \sin i$, eccentricity e, period P, absolute RV γ, longitude of periastron ω, and periastron date T_0) are drawn from a random distribution.

In order to properly account for the eccentricity distribution of known exoplanets, the random values for e are sampled from a beta distribution with $a = 0.867$ and $b = 3.03$ (Kipping 2013). Here, P, $M_p \sin i$, and T_0 are drawn from uniform distributions in log space, and γ is drawn from a normal distribution with a standard deviation of $V/2$. This is done in order to reflect our uncertainty on the absolute RV of our targets, especially in the cases with only a few RV epochs.

Synthetic RV measurements are then extracted by sampling the RV curve at the same epochs as our individual observations and assigning the same measurement errors that we have observed on each of them.

Table 4
Survey Results

Target Name	Survey Sample[a]	N_k Nights	Baseline (days)	Total S/N[b]	ς[c] ($m\,s^{-1}$)	χ^{2d}_r	S[e] ($m\,s^{-1}$)	V[f] ($m\,s^{-1}$)	N_ς[g]	V_{max}[h] ($m\,s^{-1}$) 1σ	V_{max}[h] ($m\,s^{-1}$) 3σ	3σ Mass Limit (M_{Jup})[i] HJ	WJ	CJ
RV Variables														
GJ 876	N	17	707	450	197	105.6	19	196	10.2	203	234	2.8	14	41
HD 160934 AB	Y	5	338	160	589	40.8	92	581	6.3	612	763	88	150	1100
LO Peg	Y	10	314	260	768	41.2	120	758	6.3	799	994	35	220	680
Candidate RV Variables														
BD+20 1790	Y	8	1295	200	328	21.5	71	321	4.5	345	460	32	130	820
EQ Peg A	Y,N	5	1211	410	157	25.2	31	154	4.9	165	216	7.2	18	34
GJ 3942	N	7	92	410	80	15.6	20	78	3.8	84	118	4.1	10	300
GJ 537 B	N	8	326	500	74	14.6	19	71	3.7	78	110	3.2	5.4	45
GJ 725 A	N	5	1035	380	58	14.6	15	56	3.7	61	86	5.6	130	950
GJ 740	N	11	123	630	67	17.2	16	65	4.0	71	97	1.9	3.7	140
GJ 9520	N	7	314	460	80	17.0	19	77	4.0	84	115	4.1	11	110
LHS 371	N	5	38	400	50	11.4	15	48	3.2	53	78	3.8	8	620
LHS 372	N	4	49	270	61	11.7	18	58	3.3	64	94	8.6	41	650
LHS 374	N	5	43	410	77	24.9	15	76	4.9	81	106	6.2	12	1000
Other Targets														
AG Tri	Y	10	314	240	90	5.7	38	81	2.2	94	155	3.6	16	52
AT Mic A	Y,N	9	1365	310	37	1.7	28	24	0.8	35	80	1.1	4.7	11
AT Mic B	Y,N	9	1488	320	108	3.0	62	89	1.4	111	212	2.8	13	31
au Mic	Y,N	12	1462	480	50	4.5	24	44	1.9	52	90	1.2	4.6	13
BD+01 2447	Y	7	89	290	21	1.0	21	5	0.2	17	48	1.4	41	140
BD–13 6424	Y	8	313	260	77	6.5	30	71	2.4	81	131	4.4	30	84
ε Eridani	Y	13	339	1130	30	3.8	15	26	1.7	31	56	1.1	5	17
EV Lac	N	5	193	490	44	9.0	15	41	2.8	46	70	2.5	16	36
GJ 15 A	N	14	818	490	26	1.9	19	18	0.9	25	55	0.62	2.8	8.3
GJ 3305 AB	Y	4	132	160	91	4.1	45	79	1.8	94	168	12	120	670
GJ 169	N	5	130	490	27	3.7	14	23	1.7	28	50	2.5	7.2	51
GJ 338 A	N	6	253	530	22	2.4	14	17	1.2	22	45	1.4	2	16
GJ 338 B	N	6	320	530	38	7.4	14	35	2.5	40	63	2.3	4.2	20
GJ 458 A	N	7	100	470	30	4.1	15	26	1.8	31	56	1.6	4.4	82
GJ 537 A	N	10	90	500	54	5.8	22	49	2.2	56	93	1.7	3.2	190
LHS 26	N	5	136	380	24	2.6	15	19	1.3	24	48	1.7	4.4	23
TYC 5899–26–1	Y	5	130	200	27	1.0	27	5	0.2	21	60	2.1	14	41
V1005 Ori	Y	7	131	250	47	1.5	39	26	0.7	44	105	3.6	37	120
V577 Per	Y	9	338	270	256	8.4	88	240	2.7	269	413	16	43	140

Notes. See Section 7.1 for more details on the survey results.
[a] Y: Young, N: Nearby.
[b] Combined S/N of all observed spectra for a given target, assuming that all data are photon-noise limited.
[c] Standard deviation of the per-night combined RV measurements. See Section 6 for more details.
[d] Reduced χ^2_r value of a zero-variation RV curve. See Section 6 for more details.
[e] Typical single-measurement precision of per-night combined RV measurements. See Section 6 for more details.
[f] RV variability, defined as $V = \sqrt{\varsigma^2 - S^2}$. See Section 6 for more details.
[g] Statistical significance of the RV variability V, defined as $N_\varsigma = V/S$. See Section 6 for more details.
[h] N-sigma upper limits on the RV variability term V. See Section 6 for more details.
[i] Upper mass limit above which a hot Jupiter (HZ; $P \sim 1$–10 days), warm Jupiter (WJ; $P \sim 10$–100 days), or cool Jupiter (CJ; $P \sim 100$–1000 days) would have been detected at 3σ, 95% of the time. See Section 7.1 for more details.

The synthetic RV variability term V_{synth} is then calculated for every synthetic companion, from which we derive a detection probability according to its N_ς distance from the measured V. This is done by finding the N_ς value in Equation (11) that enforces $V_{max}(N_\varsigma) = V_{synth}$. This value can then be translated to a probability, assuming that the measurement errors on V follow a normal distribution. A two-dimensional 800×800 element histogram is then constructed over the variables (P, $M_p \sin i$) in logarithmic space, which acts as a marginalization of the other orbital parameters. This two-dimensional probability distribution is then converted back to N_ς values, which can be represented as a contour plot. We display these contour plots in Figure 10 for the cases of au Mic and ε Eridani. The contour data have been smoothed with a two-pixel filter for visibility.

We define three regimes of periods P for which we determine mean upper mass limits: *hot Jupiters* (1–10 days), *warm Jupiters* (10–100 days), and *cool Jupiters* (100–1000 days). Within each

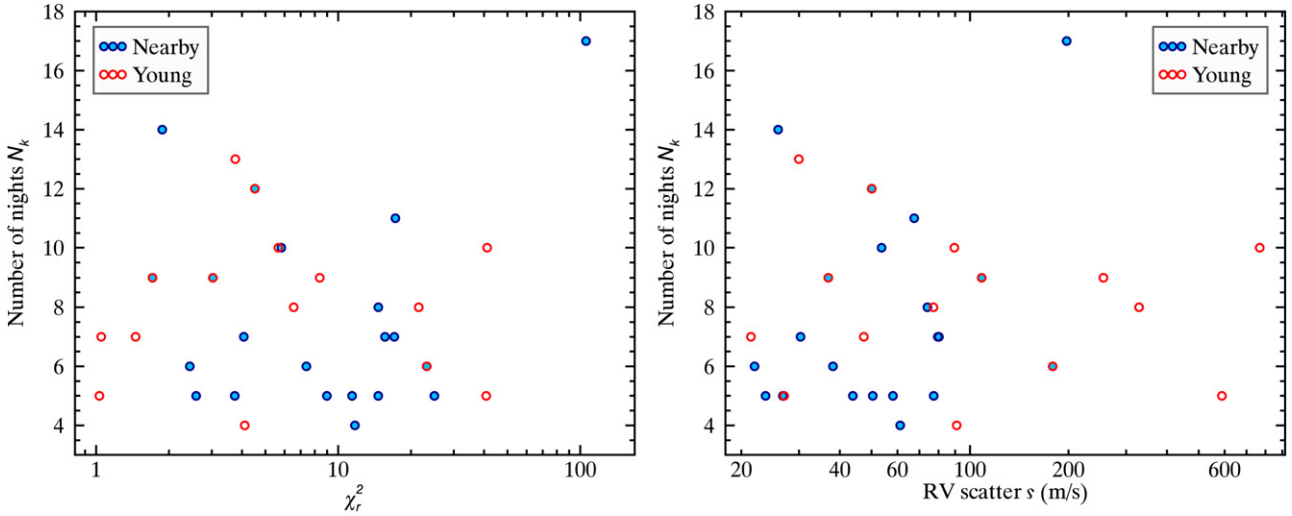

(a) Reduced chi-square value versus number of nights (b) RV scatter versus number of nights

Figure 6. Reduced χ^2 with respect to zero variation and RV scatter σ as a function of the total number of nights for which a target was observed. Young sample targets are displayed as red circles and nearby sample targets as filled blue circles. For more details, see Section 7.1.

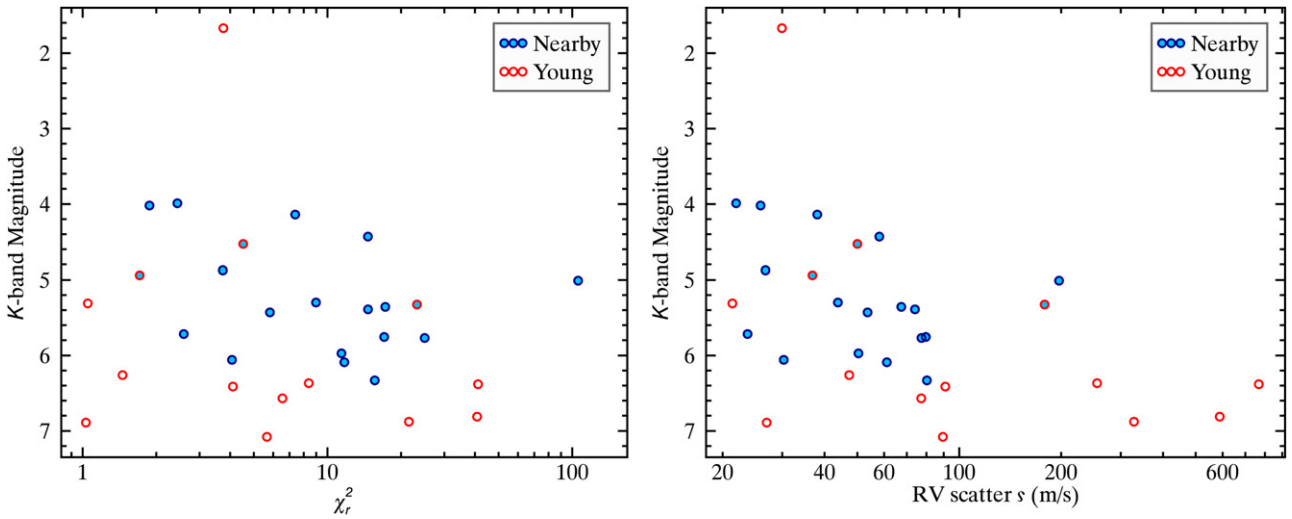

(a) Reduced chi-square value versus K-band magnitude (b) RV scatter versus K-band magnitude

Figure 7. Reduced χ^2 with respect to zero variation and RV scatter ς as a function of the 2MASS K_S-band magnitude of our targets. The χ^2_r values do not seem to be correlated with the K-band magnitude, which indicates that our RV measurement errors are realistic. The RV scatter ς, however, is correlated with the K-band magnitude, which is a natural effect of the lower S/Ns that were obtained for fainter targets. The color scheme is identical to that of Figure 6. Targets in the young sample have lower S/Ns because they were observed with smaller integration times as they were mostly observed before 2014, but also because they have fainter K-band magnitudes on average. For more details, see Section 7.1.

one of these ranges, we determine the critical mass $M_p \sin i$ at which 95% of the synthetic companions would have been detected at a 3σ confidence level. These values are reported in Table 4. These values do not allow us to contradict the existence of any companion detection that was previously reported in the literature.

7.3. Effects of Rotational Velocity and Age

To assess the impact of rotational broadening on our achievable RV precision limit, we have constructed a set of synthetic data based on our observations of GJ 15 A, which is a slow-rotating, RV-quiet star (within our survey precision), and which benefits from a large number of high-S/N observations. We have used the best fitting parameters that were obtained from the RV pipeline for each individual raw spectrum to remove the effects of the blaze function, gas cell, and telluric absorption. We then deconvolved the remaining individual stellar spectra with the appropriate LSF and used the *add_rotation.pro* IDL routine[25] to produce an artificial rotational broadening. We convolved the result with the LSF and added back the effects of the gas cell, telluric absorption, and blaze function. We generated a synthetic data set in this way for 18 values of projected rotational velocities $v \sin i$ that range from 2 to 30 km s^{-1}.

These synthetic data sets were subsequently analyzed with the MATLAB RV pipeline, as described in Section 5. We show in Figure 11(a) the resulting RV precision that was achieved as a function of projected rotational velocity. As expected, the RV

[25] Written by Russel White in 2000 December, then Greg Doppmann in 2003 July. Note that this routine is distinct from *lsf_rotate.pro* from the astrolib library at http://idlastro.gsfc.nasa.gov/ that was recently shown to contain an error (Messina et al. 2015).

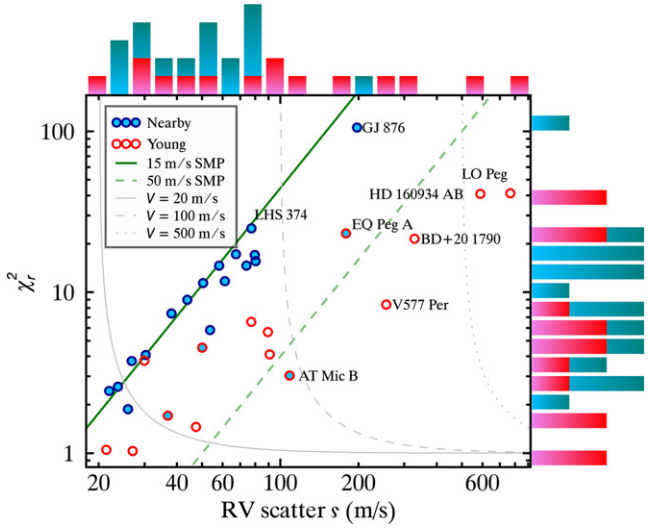

Figure 8. Reduced χ^2_r with respect to zero variation as a function of the RV scatter ς for targets in the nearby (filled blue circles) and young (red circles) samples. The solid and dashed green lines correspond to single-measurement precisions of 15 and 50 m s^{-1}, respectively. The solid, dashed, and dotted gray lines correspond to respective RV variability values V of 20, 100, and 500 m s^{-1} ($V = \sqrt{\varsigma^2 - S^2}$; see Section 6). Histogram distributions for the nearby (green bars) and young (pink bars) samples are displayed next to each plot axis. For more details, see Section 7.1.

precision starts decreasing when the projected rotational velocity gets larger than the velocity resolution of CSHELL ($c/R \sim 6.5$ km s^{-1}, where c is the speed of light in vacuum). This loss of RV precision follows a power law as a function of $v \sin i$.

We have thus modeled this effect of $v \sin i$ on the RV precision by using the quadrature sum of a constant term that represents the single-measurement precision and a two-parameter power law. The resulting fitting function is given by

$$y = \sqrt{y_0^2 + (x/\sigma_x)^{2\beta}}, \quad (15)$$

where y is the RV precision, x is the projected rotational broadening, y_0 is the RV scatter caused by all terms except rotational broadening (e.g., single-measurement precision and RV variability), and β and σ_x are the free parameters of the power law. We find best-fit values of $\sigma_x = 1.56 \pm 0.05$ km s^{-1} and $\beta = 1.70 \pm 0.02$. The best-fit solution is displayed as a red curve in Figure 11(a).

In Figure 11(b), we compare this relation to our survey results, assuming different single-measurement precisions. It can be noted that in several cases with relatively low projected rotational velocities ($v \sin i \lesssim 10$ km s^{-1}) we obtain RV precisions that do not need to include a jitter term increasing with $v \sin i$. It is, however, possible that a jitter term is the cause of the lower RV precision that we obtain for a few targets located above the 50 m s^{-1} single-measurement-precision green solid line.

The NIR jitter–$v \sin i$ relation measured by Bailey et al. (2012) for TW Hydrae members (10 ± 3 Myr; Bell et al. 2015b) is displayed as a gray dotted line in Figure 11(b). This shows that the source for the RV variability of targets within the gray region could be explained by jitter if our targets display stellar spots as significant as the young TW Hydrae population.

Such a level of jitter comparable to that of Bailey et al. (2012) is not strong enough to reproduce the RV variability of stars with known or candidate companions (GJ 876, HD 160934 AB) or the single stars V577 Per, BD+20 1790, and LHS 374. Those three targets display a level of RV variability that is thus unlikely to be explained by the combined loss of information that is due to stellar broadening and stellar jitter, but additional follow-up work will be needed to assess this with certainty.

Survey targets that have a larger projected rotational velocity show larger RV variations, as expected. This correlation is independent of the survey sample (i.e., independent of age), although younger stars are faster rotators on average. It can be noted that the large RV variability of LO Peg might be explained by RV information loss that is due to the rotational broadening of stellar lines, whereas that of EQ Peg A would require a significant jitter term at the higher end of what is admitted in the relation proposed by Bailey et al. (2012). Further observations will be required to determine whether EQ Peg A can plausibly host a substellar or planetary companion.

A fraction of the low–$v \sin i$ measurements that we have compiled from the literature might be spurious, so in these cases simply comparing $v \sin i$ to the RV variability term V is not a reliable way to determine the source of RV variability with certainty.

In Figure 12, we display RV variability as a function of the $\log R'_{HK}$ activity index. Targets in the young sample are more active on average than those in the nearby sample, as expected. The fact that we measure a relatively low RV variability for three very active targets ($\log R'_{HK} > -4.2$) provides a tentative constraint on the level of jitter in the NIR to ~25–50 m s^{-1} at ≈2.3125 μm.

7.4. Bisector Analysis

We measured the bisector slopes of CO lines in each of our individual exposures (see, e.g., Santos et al. 2001; Dravins 2008) to investigate the effect of stellar activity on our RV variable targets. We did not identify a correlation between the RV and bisector spans in any case.

However, it must be considered that the lack of a correlation might be expected given the moderate resolution ($R \approx 46{,}000$) of CSHELL and the observing setup that we have used (i.e., slit spectroscopy). Effectively, Desort et al. (2007) noted that a poor sampling of spectral lines can hinder the measurements of bisector spans; for example, a resolution of $R \approx 50{,}000$ would only be able to recover bisector span variations in targets with $v \sin i \gtrsim 6$ km s^{-1}. Slitless observations at higher resolutions would thus be warranted to guarantee that the RV variability that we measure is not associated with stellar activity.

8. DISCUSSION OF INDIVIDUAL TARGETS

8.1. RV Variable Targets

We define targets for which we measure an RV variability with a statistical significance of $N_\varsigma \geqslant 5$ as likely RV variables, and those with $3 \leqslant N_\varsigma < 5$ as candidate RV variables. All targets that fall in these categories are discussed individually in this section. More follow-up observations will be needed to determine whether any RV variability is due to a companion or to stellar activity. Although it is generally expected that the impact of stellar activity is small in the NIR regime (Martín

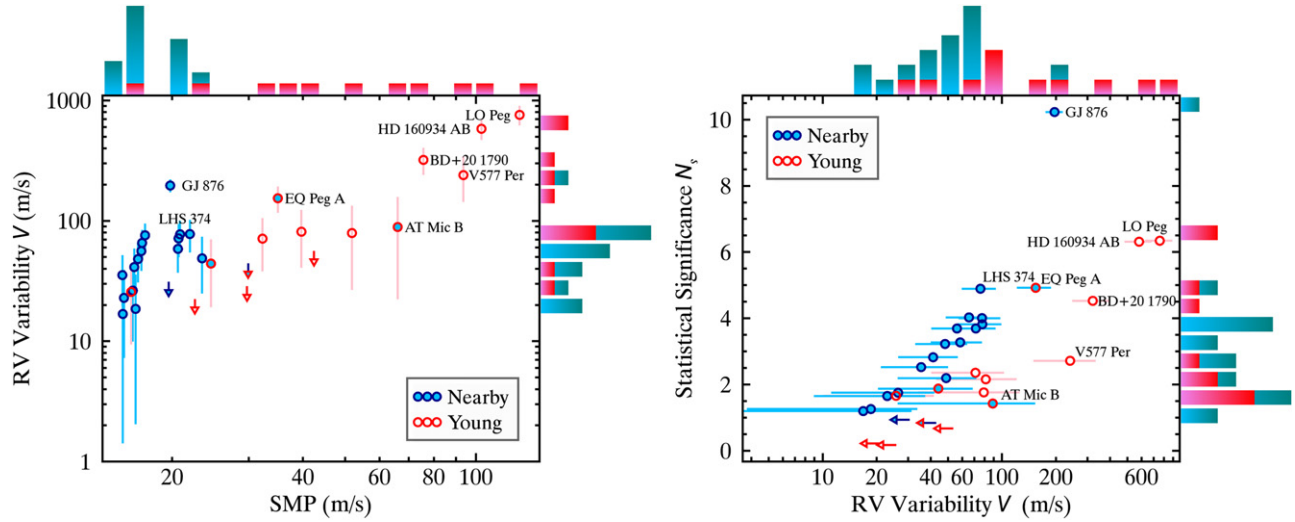

(a) RV variability versus single-measurement precision (b) Statistical significance of RV variability

Figure 9. Panel (a): RV variability V as a function of single-measurement precision for the young (red circles) and nearby (blue circles) samples. Panel (b): statistical significance as a function of the RV variability. Targets with an RV variability below 1σ are displayed as 1σ upper limits (left- or down-pointing arrows). For more details, see Section 7.1.

Table 5
Comparison with Previous Work

Target	Survey	Optical				NIR				This Work		
Name	Sample[a]	Ref.[b]	N_{data}[c]	S (m s^{-1})[d]	ς (m s^{-1})[e]	Ref.[b]	N_{data}[c]	S (m s^{-1})[d]	ς (m s^{-1})[e]	N_{data}[c]	S (m s^{-1})[d]	ς (m s^{-1})[e]
AG Tri	Y	…	…	…	…	1	14	55	98	10	38	90
AT Mic A	Y,N	…	…	…	…	1	14	50	151	9	28	37
AT Mic B	Y,N	…	…	…	…	1	14	55	207	9	62	108
au Mic	Y,N	…	…	…	…	1	14	50	125	12	24	50
BD+01 2447	Y	2	13	80	100	…	…	…	…	7	21	21
BD+20 1790	Y	**3**–5	61	5.5	580	…	…	…	…	8	71	328
ϵ Eri	Y	6	33	12.0	15.3	…	…	…	…	13	15	30
EV Lac	N	…	…	…	…	1	20	50	115	5	15	44
GJ 15 A	N	7	117	0.6	3.21	…	…	…	…	14	19	26
GJ 3305 AB	Y	8	3	20	550	1	5	50	457	4	45	91
GJ 876	N	**9**–13	162	2.0	162	…	…	…	…	17	19	197
GJ 725 A	N	…	…	…	…	1	18	50	51	5	15	58
V1005 Ori	Y	…	…	…	…	1	6	55	103	7	39	47

Notes. See Section 7.1 for more details.
[a] Y: Young, N: Nearby.
[b] When multiple references are listed, the one in bold has presented the highest overall RV precision; data presented in the following columns are obtained from this reference.
[c] Total number of RV epochs.
[d] Typical single-measurement precision.
[e] RV scatter (analogous to ς in this paper).
References. (1) Bailey et al. (2012), (2) Paulson & Yelda (2006), (3) Hernán-Obispo et al. (2015), (4) Figueira et al. (2010), (5) Hernán-Obispo et al. (2010), (6) Campbell et al. (1988), (7) Howard et al. (2014), (8) Elliott et al. (2014), (9) Rivera et al. (2010), (10) Marcy et al. (1998), (11) Marcy et al. (2001), (12) Delfosse et al. (1998a), (13) Rivera et al. (2005b).

et al. 2006; Reiners et al. 2010), it has also been shown by Reiners et al. (2013) that, under certain configurations of stellar spots and magnetic fields, the effect of jitter could in fact increase with wavelength.

GJ 876 (HIP 113020) is an M4 low-mass star (Reid et al. 1995; mass estimate 0.32 $M_\odot$; Rivera et al. 2005b) located at 4.69 ± 0.05 pc (van Leeuwen 2007). Its low rotation rate and weak magnetic activity suggest an age older than ~0.1 Gyr. Its kinematics place it in the young disk population (Correia et al. 2010), but this does not put a strong constraint on its age (i.e., $\lesssim$5 Gyr, Leggett 1992).

Using the proper motion ($\mu_\alpha \cos\delta = 959.84 \pm 3.36$ mas yr^{-1}; $\mu_\delta = -675.33 \pm 1.68$ mas yr^{-1}) and parallax measurements of van Leeuwen (2007) along with the systemic RV measurement of -1.59 ± 0.18 km s^{-1} (Nidever et al. 2002) with the BANYAN II tool (Malo et al. 2013; Gagné et al. 2014), we obtain a significant probability ($P = 85.1\%$) that this system is a member of the β Pictoris moving group, which is comparable to its other bona fide members (Gagné et al. 2014). Its *UVW* space velocity and *XYZ* galactic position place it at 5.05 ± 1.80 km s^{-1} and 13.3 ± 15.9 pc from the locus of known β Pictoris moving group members. The probability of a

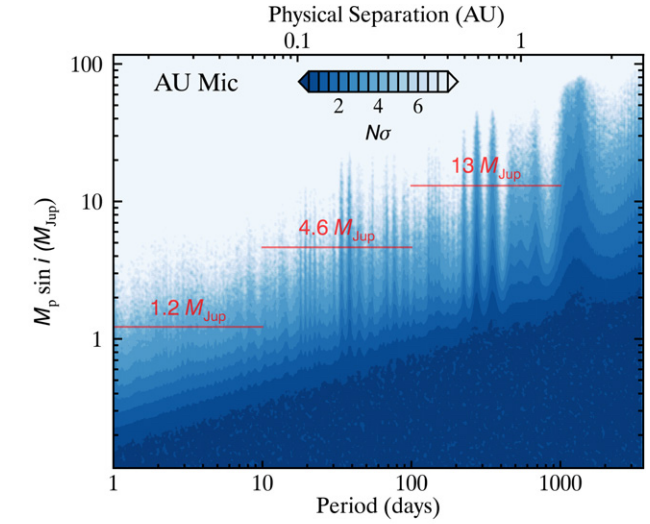

(a) AU Mic

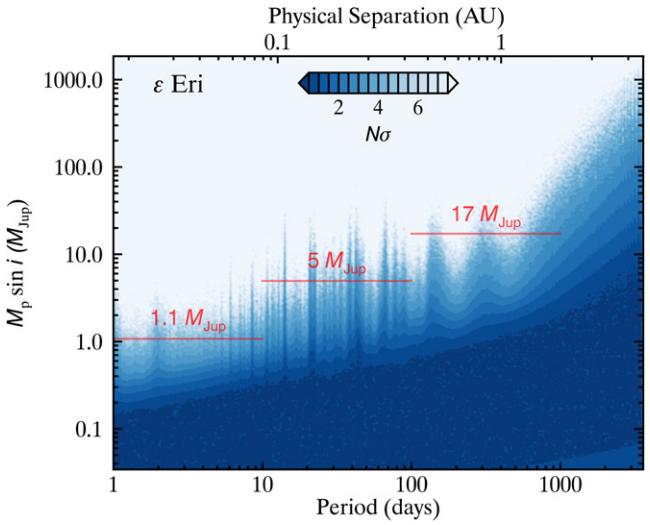

(b) ε Eridani

Figure 10. Rejection statistical significance of synthetic companions from our observed RV variation V, RV precision, and temporal sampling as a function of companion mass $M_p \sin i$ and period, for au Mic (a) and ε Eridani (b). Lighter-colored regions correspond to companion configurations that are safely rejected with our observations. We display in red the upper mass limits where 95% of the synthetic companions would have been detected at a 3σ significance in three distinct period regimes. See Section 7.2 for more details. A figure set is available in the online version displaying similar figures for all of our survey targets.

(The complete figure set (33 images) is available online.)

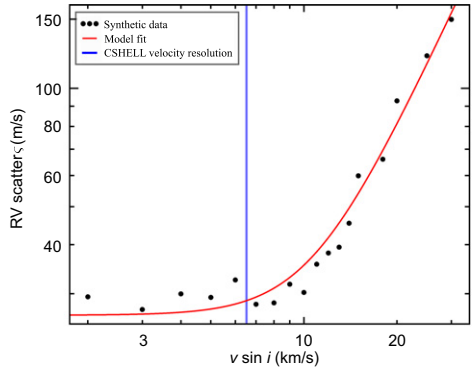

(a) Effect of $v \sin i$ on synthetic GJ 15 A RV precision

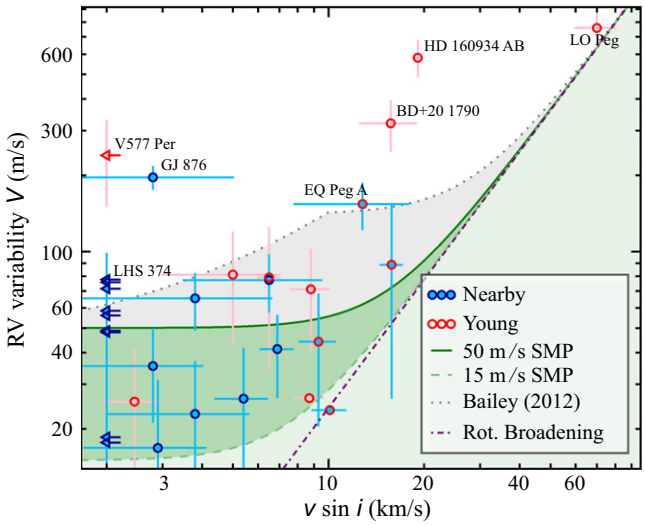

(b) RV variability and stellar jitter

Figure 11. Panel (a): RV scatter ς as a function of the synthetic rotational velocity broadening of GJ 15 A data (black circles). The red line corresponds to a best-fit power law (see Section 7.3). The blue line corresponds to the velocity resolution of a single CSHELL spectrum ($c/R \sim 6.5$ km s^{-1}). Panel (b): RV variability V as a function of the measured projected rotational velocity $v \sin i$ for the nearby (filled blue circles) and young (red circles) samples. Upper limits are displayed with left-pointing arrows. The purple dash-dotted line represents the effect of information loss from rotational velocity alone (extrapolated from the synthetic relation described in Section 7.3). The dashed (solid) green line represents the quadrature sum of a 15 m s^{-1} (50 m s^{-1}) single-measurement precision and information loss from $v \sin i$. We display the quadrature sum of a 15 m s^{-1} single-measurement precision with the $v \sin i$–jitter relation of Bailey et al. (2012) as a dotted gray line. It can be noted that the targets that we flag as RV variables lie outside of the NIR jitter region defined by Bailey et al. (2012), which is an indication that their RV variability might not be due to stellar activity. For more details, see Section 7.3.

random interloper at such spatial and kinematic distances from the locus of the group (counting both young and old stars) is only ≈1.3% (Gagné et al. 2014). However, there are several indications in the literature that this system is old. For example, Poppenhaeger et al. (2010) measured a low X-ray luminosity of $\log L_X = 26.48 \pm 0.13$, Rivera et al. (2005a) measured a large rotation period of 96.7 days and a low jitter of ∼3 m s^{-1}, and Hosey et al. (2015) showed that it is very quiet with variation amplitudes of only 17.2 mmag in the optical. Its absolute magnitude is about 0.7 mag brighter than the main sequence, which could be an indication of youth, but this can be explained by its high metallicity alone (e.g., Neves et al. 2013 measure [Fe/H] ≈ 0.12–40 dex). It is therefore most likely that GJ 876 is an old interloper to the β Pictoris moving group rather than a member because its age is not reconcilable with that of the group (24 ± 3 Myr; Bell et al. 2015a), and a star must display both consistent kinematics and a consistent age before it can be considered as a new moving group member (Song et al. 2002; Malo et al. 2013).

Marcy et al. (1998) and Delfosse et al. (1998a) have identified a 227 m s^{-1} RV signal corresponding to GJ 876 b, a Jovian planet ($M_p \sin i \approx 2.1\,M_{Jup}$) on an eccentric ($e = 0.27 \pm 0.03$) 60.85 ± 0.15 day orbit at 0.21 au around GJ 876. Marcy et al. (2001) subsequently discovered GJ 876 c, a $M_p \sin i \approx 0.6\,M_{Jup}$ planet in 2:1 resonance with GJ 876 b at 0.13 au and on a 30.1 day orbit around GJ 876. Rivera et al.

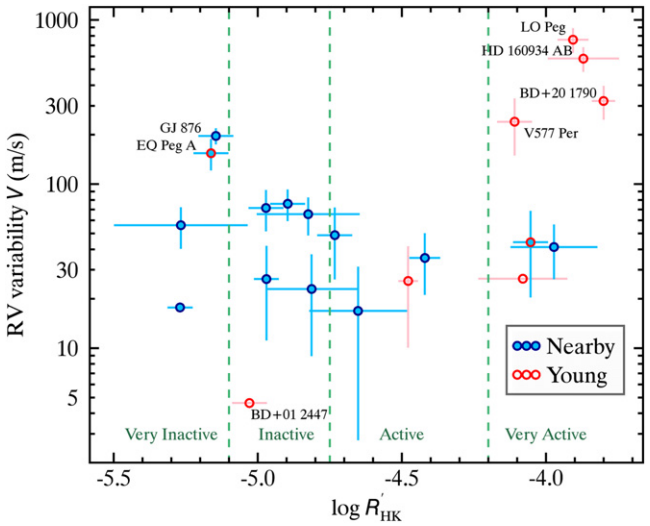

Figure 12. Activity index $\log R'_{HK}$ as a function of RV variability V for our survey samples. The fact that three very active targets ($\log R'_{HK} > -4.2$) display a low RV variability of ~25–50 m s^{-1} is a tentative indication for the level of NIR RV jitter. See Section 7.3 for more details.

(2005b) then discovered GJ 876 d, a third, $M_p \sin i \approx 5.9\,M_\oplus$ planet on a 1.9 day orbit around GJ 876.

Correia et al. (2010) predicted the possible existence of a low-mass ($<2\,M_\oplus$) planet in 4:1 orbital resonance with GJ 876 b that could explain how the high eccentricity ($e = 0.14$) of the orbit of GJ 876 d could have survived for more than ≈1 Myr, but the existence of such a planet has not been confirmed yet. Finally, Rivera et al. (2010) confirmed the existence of a fourth planet, GJ 876 e, on a 126.6 day orbit and a minimum mass of $M_p \sin i = 12.9 \pm 1.7\,M_\oplus$.

We followed GJ 876 as part of the nearby sample over 17 nights spanning >700 days with a typical S/N ≈ 170 per night and recovered it as an RV-variable target with $V = 196 \pm 19$ m s^{-1}, which is consistent within 1.6σ with the RV amplitude measured by Marcy et al. (1998). Furthermore, we find $V_{\max}(N_\varsigma = 3) = 234$ m s^{-1}, which is also consistent with measurements in the literature.

We used the Systemic 2 software[26] (Meschiari et al. 2009, 2012) to identify periodic signals in our RV curve that includes 17 epochs spanning ~1.9 years. We identified a strong signal at $P \approx 61.5$ days associated with a false-alarm probability of only 3.5×10^{-4}%. Fitting an orbital solution with the Simplex algorithm yielded the orbital parameters listed in Table 6 and the orbital phase curve displayed in Figure 13. There is one data point (phase ~313° or 2011 July 10) that is a significant outlier to this orbital fit, but it was obtained in bad weather conditions with a seeing above 3″.

The period, planetary mass, and eccentricity are remarkably consistent with the values associated with GJ 876 b in the literature (e.g., Marcy et al. 1998), except for the argument of periastron ω, which is significantly different. This eccentric solution is in fact a combined effect of the RV influence of the two planets GJ 876 b and GJ 876 c on the host star, rather than a physical orbit. It is therefore expected that this artificial value for ω librates with time. Furthermore, this also means that our orbital parameters can only be meaningfully compared to those of Marcy et al. (1998), who also fitted a single orbit to

[26] http://github.com/stefano-meschiari/Systemic2

Table 6
Orbital Solution for GJ 876 b

Parameter	Marcy et al. (1998)	This Paper
Orbital period P (days)	60.85 ± 0.15	61.23 ± 0.29
Eccentricity e	0.27 ± 0.03	0.24 ± 0.10
Lon. of periastron ω (deg)	24 ± 6	209 ± 25
Periastron date T_0 (JD-2.4 × 10^6)	50301.0 ± 1.0	55452.7 ± 4.6
Planet's mass $M_p \sin i$ ($M_{\rm Jup}$)	2.11 ± 0.20	2.73 ± 0.38
Semimajor axis a (au)	0.21 ± 0.01	0.2041 ± 0.0007

Note. See Section 8.1 for more details.

GJ 876 bc. To our knowledge, our data thus provide the first multiwavelength confirmation of the planet GJ 876 bc, thus confirming that the RV signal cannot likely be explained by stellar jitter.

Once the periodic signal of GJ 876 bc is subtracted from our data, our long-term precision does not allow us to detect any additional signal that could be associated with the other known planets orbiting GJ 876 (see Figure 13). Our analysis, however, demonstrates that we are able to detect planets with the characteristics of GJ 876 bc using a 3 m–class telescope and relatively inexpensive equipment.

HD 160934 AB (HIP 86346) is a young and active M0-type low-mass star member of the AB Doradus moving group (Zuckerman et al. 2004; Malo et al. 2013), located at 33.1 ± 2.2 pc (van Leeuwen 2007). It has been confirmed as a close (0.″12) SB1 binary in an eccentric ($e \approx 0.8$), 17.1 year orbit both by the RV (Gálvez et al. 2006) and direct imaging (Hormuth et al. 2007) methods. Its individual components have estimated spectral types of M0 and M2–M3 (Gálvez et al. 2006) and estimated masses of $0.69\,M_\odot$ and $0.57\,M_\odot$ (Hormuth et al. 2007).

Griffin (2013) used their RV measurements as well as those reported by López-Santiago et al. (2010), Maldonado et al. (2010), and Gizis et al. (2002) to derive an orbital solution for HD 160934 AB. They assumed an orbital inclination of 82.3 ± 0.°8, which was obtained from direct-imaging data (Hormuth et al. 2007; Lafrenière et al. 2007; Evans et al. 2012) and stellar masses of 0.65 and $0.5\,M_\odot$, respectively.

We followed HD 160934 AB as part of the young sample for a total of five nights spanning 338 days with a typical S/N of 150 per night and recovered it as an RV variable with $V = 581 \pm 92$ m s^{-1}. We find a strong linear trend of 1853 ± 163 m s^{-1} yr^{-1} in its RV curve, but the reduced χ^2_r value remains high (11.3) even after subtracting a linear curve.

In Figure 14, we compare our RV measurements with those reported by Griffin (2013), and we find that they are consistent with the orbital solution that they propose, but our limited time baseline only allows us to detect a linear trend in our RV data.

LO Peg (HIP 106231) is yet another young, active K8 low-mass star member of the AB Doradus moving group (Zuckerman et al. 2004; Malo et al. 2013), located at 24.80 ± 0.65 pc (van Leeuwen 2007). Measurements of polarization suggest the possibility that a circumstellar envelope remains around LO Peg or that significant brightness inhomogeneities exist on its surface (Pandey et al. 2009). This target has the largest rotational velocity of our sample with $v \sin i = 70 \pm 10$ km s^{-1} (Głębocki & Gnaciński 2005) and a rotation period of 0.42 days (Messina et al. 2010).

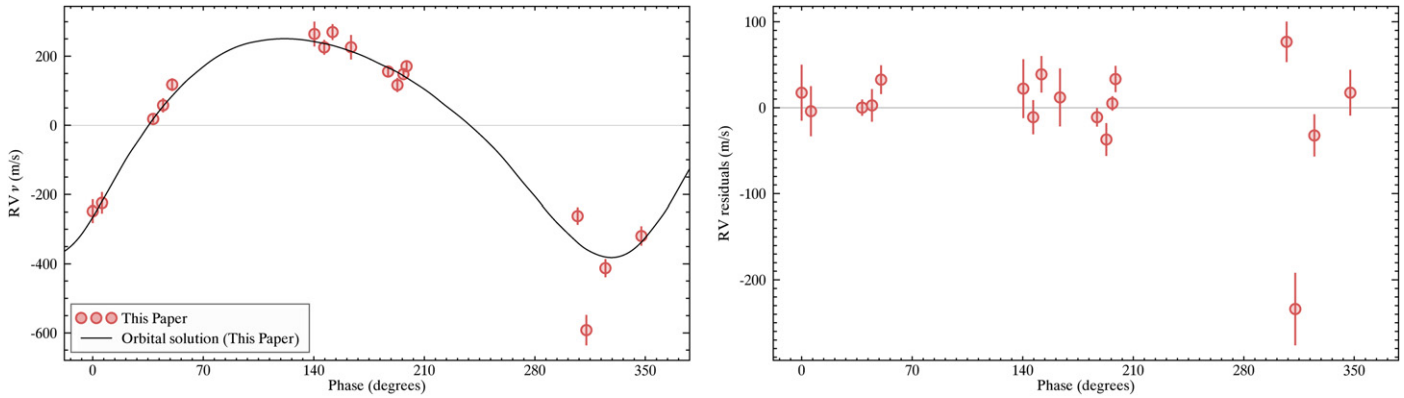

(a) Orbital Fit to GJ 876 b (b) Residuals for GJ 876 b

Figure 13. Panel (a): orbital fit of GJ 876 b (thick black line) to our RV measurements (red circles). We recover orbital parameters that are fully consistent with those reported in the literature. The outlier data point with a phase of ∼313° was obtained in bad weather conditions on 2011 July 10 with a seeing above 3″. Panel (b): residuals after the subtraction of GJ 876 b. Our current data do not allow us to detect the other known planetary companions to GJ 876. For more details, see Section 8.1.

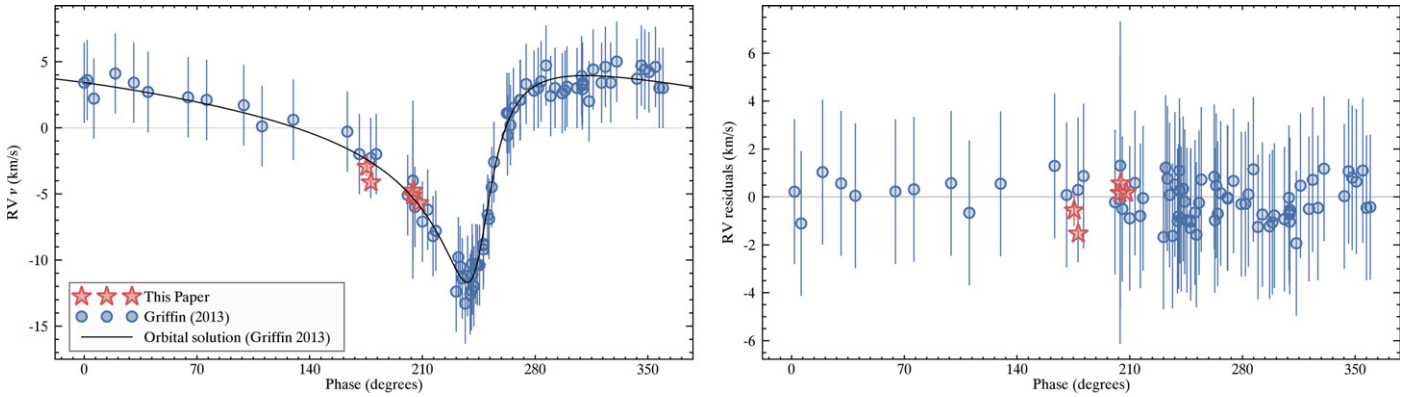

(a) Orbital Fit to HD 160934 AB (b) Residuals for HD 160934 AB

Figure 14. Panel (a): comparison of our HD 160934 AB RV measurements (red stars) with those in the literature (blue circles) and the reported orbital solution of the system (thick black line). Our measurements are consistent with the known orbit. Panel (b): residuals after the subtraction of the known orbit of the HD 160934 AB system. For more details, see Section 8.1.

We followed LO Peg as part of the young sample for a total of 10 nights spanning 314 days with a typical S/N ∼ 100 and identified it as an RV variable with $V = 758 \pm 120\,\mathrm{m\,s^{-1}}$. The RV variability is not well fit by a linear trend, and it is thus very unlikely that it can be explained by a massive stellar companion. However, it is possible that the loss of RV information due to rotational broadening of the stellar lines is the only cause of this large RV variation (see Figure 11(b)). Additional RV follow-up using a larger spectral grasp might be able to mitigate this effect.

8.2. Candidate RV Variable Targets

BD+20 1790 is a fast-rotating ($v \sin i = 16 \pm 3\,\mathrm{km\,s^{-1}}$; White et al. 2007), active K5-type (Reid et al. 2004) member of the AB Doradus moving group (López-Santiago et al. 2006; Malo et al. 2013), located at 38.8 ± 2.0 pc (Shkolnik et al. 2012).

Hernán-Obispo et al. (2010) identified RV variability at an amplitude of $\approx 1.8\,\mathrm{km\,s^{-1}}$ in the optical. Based on its photometric variability as well as analyses of its bisector and spectroscopic indices of chromospheric activity, they interpret the RV signal as the probable signature of a close-in (0.07 au), massive (6–7 M_{Jup}) planet on a 7.8 day orbit rather than the effect of chromospheric activity. They note that two solutions of different eccentricities could fit the RV data ($e = 0.05 \pm 0.02$ or $e = 0.14 \pm 0.04$).

Figueira et al. (2010) subsequently presented evidence against the interpretation of a planetary companion, by showing that the RV signal correlates with the bisector span of the stellar lines, and by obtaining a different RV variation amplitude of $460\,\mathrm{m\,s^{-1}}$ with a periodicity of 2.8 days that corresponds to the rotation period of the star.

Hernán-Obispo et al. (2015) presented a reanalysis of the RV variations of BD+20 1790 by removing the RV signal that is due to jitter using a Bayesian method and suggested that the RV variation is due both to stellar activity and a planetary companion. They furthermore suggest that the bisector span–RV correlation reported by Figueira et al. (2010) was due to flare events and that the correlation disappears in flare-free data. They present new orbital parameters for the candidate BD+20 1790 b that are similar to those reported by Hernán-Obispo et al. (2010), except that they find a more eccentric solution ($e \approx 0.1$ to $e \approx 0.2$).

We observed BD+20 1790 as part of the young sample for a total of eight nights spanning ≈3.5 years with a typical S/N ≈ 70 per night and recovered it as a candidate RV variable, with $V = 321 \pm 71\,\mathrm{m\,s^{-1}}$. Our RV curve is consistent with variations at an amplitude of $\approx 1\,\mathrm{km\,s^{-1}}$ (see Figure 3(g)), thus

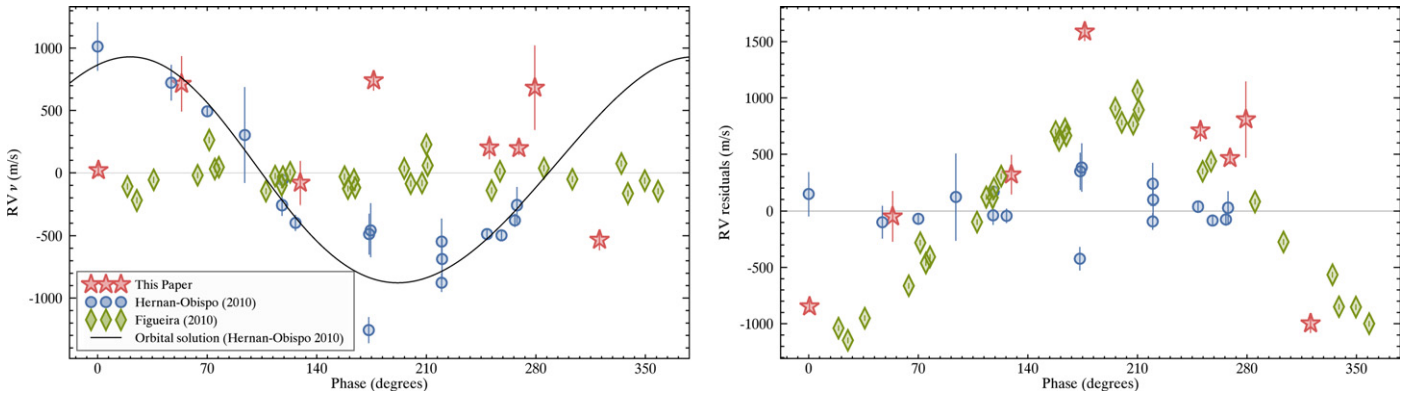

(a) Orbital Fit to BD+20 1790 (b) Residuals for BD+20 1790

Figure 15. Panel (a): comparison of our RV measurements (red stars) with those reported by Hernán-Obispo et al. (2010; blue circles) and Figueira et al. (2010; green diamonds), as well as the suggested orbital parameters associated with the purported planet BD+20 1790 b (see Solution 1 with $e = 0.05$ in Hernán-Obispo et al. 2010). We find an RV scatter that is consistent with that of Hernán-Obispo et al. (2010), suggesting that there might be an RV signal not associated with stellar activity since the amplitude does not depend on wavelength, but our data do not match the orbital solution suggested by Hernán-Obispo et al. (2010) or any of those reported in the literature for the candidate BD+20 1790 b. Panel (b): residuals after the subtraction of the orbit suggested by Hernán-Obispo et al. (2010). For more details, see Section 8.2.

providing further indication that the RV variability might not be explained by chromospheric activity alone. However, our data are inconsistent with any of the orbital solutions presented by Hernán-Obispo et al. (2010, 2015) (e.g., see Figure 15).

Using any combination of our data set or the data of Hernán-Obispo et al. (2010) and Figueira et al. (2010), we cannot identify any statistically significant periodicity. More follow-up observations will thus be needed to assess whether the RV variations could be caused by a companion or not. It is unlikely that the RV variability of BD+20 1790 could be explained by the loss of RV that was due to its fast rotation or to stellar jitter (see Figure 11(a)).

EQ Peg A (GJ 896 A; HIP 116132) is a young, M3.5-type (Newton et al. 2014; Davison et al. 2015), flaring low-mass star located at 6.58 ± 0.16 pc (van Leeuwen 2007). Zuckerman et al. (2013) suggested that it is a member of the Octans-Near association.

EQ Peg A has a stellar companion (EQ Peg B) at an angular distance of $\approx 5\farcs5$ ($\approx$36 au), which is an M4.0-type flare star (Davison et al. 2015).

We followed EQ Peg A as part of the young sample for a total of six nights spanning $\approx$3.3 years with a typical $S/N \approx 170$ per night and recovered it as a candidate RV variable with $V = 175 \pm 37$ m s^{-1}. This RV variability cannot be explained by a long-term linear trend that could be produced by EQ Peg B. The loss of RV information because of rotational broadening is not important enough to explain this large RV variability, but the addition of a jitter term at the larger end of the distribution measured by Bailey et al. (2012) could be sufficient (see Figure 11(a)). Additional follow-up will be required to address this.

GJ 3942 (HIP 79126) is a nearby M0 star (Vyssotsky 1956) located at 16.93 ± 0.30 pc (van Leeuwen 2007). No precise RV measurements were reported in the literature as of yet.

We followed GJ 3942 as part of the nearby sample for a total of seven nights spanning 92 days, at a typical $S/N \approx 150$ per night. We identified it as a candidate RV variable with $V = 78 \pm 20$ m s^{-1}. A high-S/N follow-up over a longer baseline will be useful to determine whether this RV signal is physical or not.

GJ 537 B (HIP 68588 B) is a nearby M0 star (Gaidos et al. 2014) located at 12.3 ± 0.9 pc (Jenkins 1952). It is a companion to GJ 537 A at an angular separation of $\approx 2\farcs9$.

We followed GJ 537 B as part of the nearby sample for a total of eight nights spanning a total of 326 days with a typical $S/N \approx 180$ per night. We recovered it as a candidate RV variable with $V = 71 \pm 19$ m s^{-1}. Additional follow-up measurements will be needed to determine the nature of this likely RV variability.

GJ 725 A (HIP 91768) is a nearby (3.57 ± 0.03 pc; van Leeuwen 2007), quiet and slowly rotating M3-type star (Jenkins et al. 2009).

Nidever et al. (2002) have shown that GJ 725 A is stable within 100 m s^{-1} on a baseline of $\approx$3 years, and Endl et al. (2006) further constrained its RV stability by obtaining a scatter of only 7.4 m s^{-1} in their RV measurements over a baseline of $\approx$7 years.

GJ 725 A has a comoving M3.5-type (Jenkins et al. 2009) companion (GJ 725 B; HIP 91772) at an angular separation of $\approx 13\farcs3$. Endl et al. (2006) report that they detect a linear RV slope of 6.99 ± 0.86 m s^{-1} yr^{-1} in the GJ 725 A data over a 7.09 year baseline, which they interpret as a small portion of its orbit around the center of mass of GJ 725 AB.

We followed GJ 725 A as part of the nearby sample for a total of five nights that spanned 2.8 years with a typical $S/N \approx 170$ per night and identified it as a candidate RV variable with $V = 56 \pm 15$ m s^{-1}. Our data are well fit by a linear trend with a slope of 35 ± 5 m s^{-1} yr^{-1}.

Using the projected separation of GJ 725 AB ($\approx$47 au) and assuming typical masses of $\approx 0.36\,M_\odot$ and $\approx 0.3\,M_\odot$ that correspond to their respective spectral types of M3 and M3.5 (Reid & Hawley 2005; Kaltenegger & Traub 2009), their orbital period should be $P \approx 400$ years. This corresponds to a tangential velocity of $v \approx 1.75$ km s^{-1} as measured from the center of mass in the case of a circular orbit. In the extreme case where the orbit is seen edge-on from Earth, we could expect a change of RV of up to $\approx$25 m s^{-1} yr^{-1} per year. Our RV slope measurement is slightly larger than this, which could be an indication that the orbit of GJ 725 AB is eccentric (e.g., $e \gtrsim 0.155$ would be sufficient).

We thus measure an RV slope that is consistent with the orbit of GJ 725 AB as long as it is slightly eccentric, but in the ≈9 years that separate our measurements from those of Endl et al. (2006), it might seem surprising that the RV slope has changed by $\approx 28\,\mathrm{m\,s^{-1}\,yr^{-1}}$. Assuming that both our measurements are consistent with the orbit of GJ 725 AB indeed puts a much stronger constraint on its eccentricity, at $e \gtrsim 0.435$.

GJ 740 (HIP 93101) is a nearby, weakly active M0.5 star (Reiners et al. 2012) located at 10.91 ± 0.18 pc (van Leeuwen 2007). No precise RV measurements were reported in the literature as of yet.

We followed GJ 740 as part of the nearby sample for a total of 11 nights spanning 123 days with a typical S/N ≈ 190 per night. We recovered it as a candidate RV variable with $V = 65 \pm 16\,\mathrm{m\,s^{-1}}$. A high-S/N follow-up over a longer baseline will be useful to determine whether this RV signal is physical or not. We note a significant linear trend in our RV curve with a slope of $-415 \pm 44\,\mathrm{m\,s^{-1}\,yr^{-1}}$, but we obtain a high reduced χ^2_r value of ≈10.2 from a linear fit, which indicates that the scatter is still relatively high even when the linear trend is subtracted. We obtain $\varsigma = 46.3\,\mathrm{m\,s^{-1}}$ and $V = 43.4 \pm 16.3\,\mathrm{m\,s^{-1}}$ ($N_\varsigma = 2.7$) after the subtraction, which would not qualify for an additional statistically significant variation under our criteria.

GJ 9520 (HIP 75187) is a nearby M1.5-type (Reid et al. 2004) star located at 11.41 ± 0.24 pc (van Leeuwen 2007). No precise RV measurements were reported in the literature for this star as of yet.

We followed GJ 9520 as part of the nearby sample for a total of seven nights spanning 314 days with a typical S/N ≈ 170 per night. We recovered it as a candidate RV variable with $V = 77 \pm 19\,\mathrm{m\,s^{-1}}$. Additional follow-up will be needed to determine whether this RV signal is physical or not.

LHS 371 (HIP 70529) and *LHS 372* (HIP 70536) form a binary stellar system located at 16.36 ± 0.40 pc (van Leeuwen 2007) with respective spectral types of M0 and M1 (Gaidos et al. 2014), and they are separated by ≈45″. No precise RV measurements for either of the two components were reported in the literature as of yet.

We followed both LHS 371 and LHS 372 as part of the nearby sample for a total of five and four nights that span 38 and 49 days with typical S/N precisions of ≈180 and 135 per night, respectively. Both components were identified as candidate RV variables, with $V = 48 \pm 15\,\mathrm{m\,s^{-1}}$ (LHS 371) and $V = 58 \pm 18\,\mathrm{m\,s^{-1}}$ (LHS 372). Subsequent follow-up will be needed to determine whether this RV variation is physical.

LHS 374 (HIP 70956) is a slow-rotating and chromospherically inactive, nearby M0 star (Gaidos et al. 2014) located at 16.99 ± 0.42 pc (van Leeuwen 2007). No precise RV measurements were reported in the literature for this star as of yet.

We followed LHS 374 as part of the nearby sample for a total of five nights spanning 43 days with a typical S/N ≈ 180 and recovered it as a candidate RV variable with $V = 76 \pm 15\,\mathrm{m\,s^{-1}}$. Subsequent follow-up will be needed to determine whether this RV variation is physical.

8.3. Likely Linear Trends in RV Curves

The presence of a massive companion at a large-enough separation can induce a linear variation in our RV curves with a period that possibly exceeds our temporal baseline coverage of a given target. The criteria defined above, which are based on the scatter of RV points around the mean, will be less sensitive to detecting such variations in a given RV curve, compared with one where at least one period is sufficiently sampled. In order to identify such candidate RV variables, we have fit a linear slope to all RV curves presented in this work using the IDL routine *mpfitfun.pro* written by Craig B. Markwardt.[27] In this section, we focus on the targets for which a linear fit yielded a reduced chi-square of at most 3, corresponding to a non-null RV slope at a statistical significance of at least 3σ. These criteria have yielded three likely RV variable targets.

GJ 458 A is a nearby M0 star (Reid et al. 2004) located at 15.52 ± 0.34 pc (van Leeuwen 2007). It has an M3-type companion (GJ 458 B, or BD+55 1519 B; Hawley et al. 1997) at an angular distance of ≈14.″7.

We followed GJ 458 A as part of the nearby sample for a total of seven nights spanning 100 days with a typical S/N ≈ 180 per night. We did not recover it as a statistically significant RV variable in terms of RV scatter on our total baseline, but its RV curve is well fit by a linear trend ($\chi^2_r = 3.0$) with a corresponding slope of $-185 \pm 50\,\mathrm{m\,s^{-1}\,yr^{-1}}$ (3.7σ significance; see Figure 4(f)).

Assuming a mass of $\approx 0.58\,M_\odot$ for GJ 458 A (Gaidos et al. 2014) and a mass of $\approx 0.36\,M_\odot$ for GJ 458 B that is typical of a field M3 star (Reid & Hawley 2005; Kaltenegger & Traub 2009) and using the projected separation of ≈228 au, we would expect a period of ≈3550 years for the orbit of the GJ 458 AB system in a case with zero eccentricity. This would be consistent with a maximal RV slope of only $\approx 1.2\,\mathrm{m\,s^{-1}\,yr^{-1}}$. Only a well-aligned, extremely eccentric orbit ($e \gtrsim 0.95$) could explain this, which is highly unlikely. It is thus probable that we are not measuring the effect of GJ 458 B, but rather possibly that of an unknown, massive companion. It is unlikely that this RV signal is due to stellar jitter because this would yield a more rapidly varying random RV signal, and GJ 458 A is an inactive, slow-rotating star (Herrero et al. 2012).

GJ 3305 AB is a known 0.″093 binary low-mass M0-type (Kasper et al. 2007) member of the β Pictoris moving group located at 29.8 ± 0.8 pc. It has been identified as a 66″ common proper motion companion system to the F0-type star 51 Eridani (Feigelson et al. 2006), which itself has a $2\,M_{\mathrm{Jup}}$ planetary, T-type companion identified by the method of direct imaging (Macintosh et al. 2015). This system will thus be a very important benchmark to understand stellar and planetary properties at young ages in the near future.

Montet et al. (2015) recently led a full RV and astrometric characterization of the GJ 3305 AB pair and their orbital properties. They found a period of 29.16 ± 0.65 years, a semimajor axis of 9.8 ± 0.15 au, an eccentricity of 0.19 ± 0.02, and individual masses of 0.65 ± 0.05 and $0.44 \pm 0.05\,M_\odot$ for A and B, respectively. They compared the observed dynamical masses with evolutionary models to derive an age of 28^{+15}_{-6} Myr for the system, consistent with the age of the β Pictoris moving group (24 ± 3 Myr; Bell et al. 2015a). They, however, obtain a dynamical mass for GJ 3305 B that is discrepant with that of evolutionary models, which they suggest could be explained by the presence of an unresolved companion.

Delorme et al. (2012) have identified a potential 0.″38 companion to GJ 3305 A by direct imaging in a 2009 NACO

[27] See http://cow.physics.wisc.edu/~craigm/idl/idl.html.

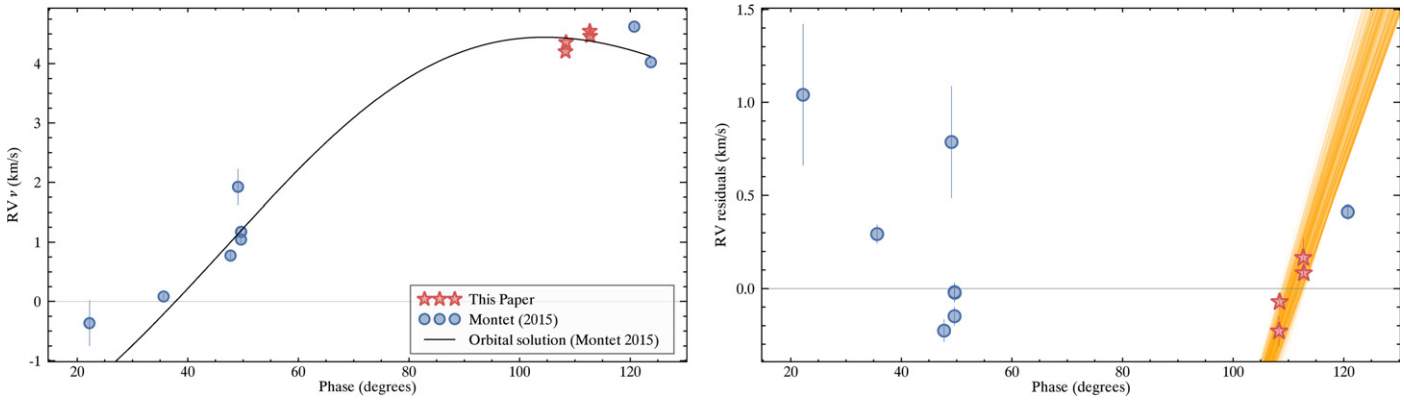

(a) Orbital Fit to GJ 3305 AB (b) Residuals for GJ 3305 AB

Figure 16. Panel (a): comparison of our RV measurements (red stars) with those reported by Montet et al. (2015) for GJ 3305 AB (blue circles) as well as their orbital solution. Panel (b): Residuals after subtracting the orbital solution of Montet et al. (2015). The linear trend (orange lines) that we measure in our RV data cannot be explained by the GJ 3305 AB orbital solution of Montet et al. (2015), but it remains to be determined whether it is due to an additional companion or not. For more details, see Section 8.3.

image in the L' band, but further observations obtained in 2012 revealed that it was not a planetary companion, but rather a speckle or a background star.

We observed the unresolved GJ 3305 AB pair during a total of four nights at a typical S/N $\approx$ 80 per night over a period of five months as part of the young sample. The RV curve of this target is well fit by a linear trend ($\chi^2_r = 1.8$) with a corresponding slope of $435 \pm 145\,\mathrm{m\,s^{-1}\,yr^{-1}}$ (3.0σ significance; Figure 3(d)).

In Figure 16, we compare our measurements with those reported by Montet et al. (2015) and find that our observed linear trend is inconsistent with the orbital solution that they suggest. To make this more apparent in the figure, we performed a 250-step Monte Carlo fitting of a linear polynomial relation to our four data points, accounting for their error bars, and displayed the resulting best fits on top of the RV residuals. It can be seen that they are significantly inconsistent with the zero-slope relation that would be expected in RV residuals randomly distributed around the orbital solution. Since our RV measurements are relative, we have applied an arbitrary shift to align our RV data with the known orbit. As a result, the only information contained in our data is this short-timescale slope that is inconsistent with the known orbit. We note that several other RV measurements from the literature also display significant short-timescale variations that are unexplained by the binary orbit, which could be indicative of an additional RV signal. More follow-up data will be needed to confirm whether there is an additional RV variability to this system that is statistically significant.

8.4. Other Noteworthy Targets

We describe in this section the targets that we did not select as candidate RV variables, but for which relevant information is available in the literature.

GJ 15 A: Howard et al. (2014) reported the detection of a 5.35 $M_\oplus$ planet in a 11.443 day orbit around GJ 15 A. Our data lack the precision and cadence necessary to detect the planet outright. However, by assuming the planet period and ephemeris reported by Howard et al. (2014), we can place a constraint on the mass of the planet with the data presented here. We used our 10 per-night RV measurements with uncertainties of $<60\,\mathrm{m\,s^{-1}}$ and phased them at an 11.443 day period and ephemeris reported by Howard et al. (2014). We averaged measurements between phases of 0–π rad and subsequently between π–2π rad. We then subtracted the results obtained from these two averages and converted this number into a semiamplitude by making use of the fact that a similar operation carried out on a sinusoidal wave (i.e., subtracting its average between phases of 0–0.5 rad and that between 0.5–1 rad) is equal to $\sqrt{3}\,K$, where K is its semiamplitude. We used the approximation that our RV measurements are evenly distributed in phase to derive $K = 8\,\mathrm{m\,s^{-1}}$. In order to quantify the uncertainty on this measurement, we computed a Monte Carlo simulation of 20 trial periods. For each trial period, we carried out the same phase-averaged measurement of the semiamplitude and measured a standard deviation of $12\,\mathrm{m\,s^{-1}}$. We thus derive a value of $K = 8 \pm 12\,\mathrm{m\,s^{-1}}$ for the RV variation semiamplitude of GJ 15 A, which corresponds to a 3σ upper limit of $<36\,\mathrm{m\,s^{-1}}$ on its RV variation, or an upper limit of $<66\,M_\oplus$ on the mass of its companion.

ε Eridani is a young K2 star located at 3.216 ± 0.002 pc (van Leeuwen 2007), for which disputed planet candidates have been reported by Campbell et al. (1988) and Quillen & Thorndike (2002), associated with RV scatters lower than $15\,\mathrm{m\,s^{-1}}$.

We followed this target as part of the young survey for a total of 13 nights spanning 339 days, with a typical S/N $\approx$ 300 per night. We did not identify it as an RV variable ($V = 26 \pm 15\,\mathrm{m\,s^{-1}}$), but we lack the long-term precision that would be needed to determine whether the signals reported by Campbell et al. (1988) or Quillen & Thorndike (2002) are spurious.

9. CONCLUSION

In this paper we report the results of a precise NIR RV survey of 32 low-mass stars with spectral types K2–M4, carried out with CSHELL and an isotopologue gas cell at the NASA IRTF, 19 of which were never followed by high-precision RV surveys. We used a novel data-reduction and RV extraction pipeline to demonstrate that we can achieve short-term photon-limited RV precisions of $\approx 8\,\mathrm{m\,s^{-1}}$ with long-term stability of $\approx 15\,\mathrm{m\,s^{-1}}$, which are unprecedented using a small telescope that is easily accessible to the community.

We used the nondetections of our survey to assign upper limits on the masses of close-in companions to our targets, and we provide the first multiwavelength confirmation of GJ 876 bc and recover orbital parameters that are fully consistent with those reported in the literature. We obtained RV curves for two binary systems (HD 160934 AB, GJ 725 AB) that are consistent with the literature, and we report that GJ 740 and GJ 458 A could be bound to unknown, long-period and massive companions. We identified seven new candidate RV variables (EQ Peg A, GJ 3942, GJ 537 B, GJ 9520, LHS 371, LHS 372, and LHS 374) with statistical significances in the 3–5σ range. Additional observations will be needed to verify whether these RV variable stars host substellar or planetary companions.

Comparing our results with the projected rotational velocities of our sample, we showed that the proposed jitter relation of Bailey et al. (2012) for young TW Hydrae members is not large enough to account for the observed RV variations of LHS 374, BD+20 1790, and V577 Per. The probability that targets in the nearby sample display larger RV variations than those in the young sample is 54%; the two samples are thus not significantly different in this regard. We find that very active stars in our survey can display RV variabilities down to $\sim$25–50 m s^{-1}, providing a constraint on the effect of jitter in the NIR.

In the near future, iSHELL will be mounted on the IRTF with a methane gas cell similar to that used in this work; the improved spectral grasp ($\approx$50 times larger), resolution ($R \approx 70{,}000$), and instrumental sensitivity will achieve RV precisions of $\lesssim$5 m s^{-1} that will allow the detection of super-Earth planets ($\gtrsim 13\,M_{\oplus}$) near the habitable zone of mid-M, low-mass stars in the solar neighborhood. Achieving such precisions on active, very-low-mass stars using optical facilities will be challenging, so NIR RV techniques will play a key role in characterizing Earth-like planets in the habitable zone of low-mass stars. These will serve as a crucial complement to transiting exoplanet studies because the combination of both the RV and transit methods will provide a measurement of the mean planet density and put strong constraints on the physical properties of future Earth-like discoveries.

We thank the anonymous referee who provided valuable comments and suggestions that significantly improved the overall quality of this paper. We thank Jason Wright, Julien Rameau, Étienne Artigau, David Montes, and Noé Aubin-Cadot for useful comments and discussions, as well as Keeyoon Sung, Sam Crawford, Brian Drouin, Edgardo Garcia-Berrios, Nathan S. Lewis, and S. Lin for precious help in the construction and setup of the methane isotopologue gas cell. We thank the IRTF staff for their collaboration and help throughout this project, in particular John Rayner, Lars Bergknut, Bobby Bus, and the telescope operators. This work was supported in part through an Infrared Processing and Analysis Center (IPAC) fellowship, a grant from the Fond de Recherche Québécois—Nature et Technologie and the Natural Science, a grant from the Engineering Research Council of Canada, an iREx postdoctoral fellowship, and a JPL Research and Technology Development Grant. This work was performed in part under contract with the California Institute of Technology (Caltech)/Jet Propulsion Laboratory (JPL) funded by the National Aeronautics and Space Administration (NASA) through the Sagan Fellowship Program executed by the NASA Exoplanet Science Institute. This research made use of the SIMBAD database and VizieR catalog access tool, operated at the Centre de Données Astronomiques de Strasbourg, France (Ochsenbein et al. 2000); data products from the Two Micron All Sky Survey (2MASS; Kirkpatrick et al. 2003; Skrutskie et al. 2006), which is a joint project of the University of Massachusetts and IPAC/Caltech, funded by NASA and the National Science Foundation; the Extrasolar Planets Encyclopaedia (exoplanet.eu), which was developed and is maintained by the exoplanet TEAM; the NASA Exoplanet Archive, which is operated by Caltech, under contract with NASA under the Exoplanet Exploration Program; the NASA/IPAC Infrared Science Archive (IRSA), which is operated by JPL, Caltech, under contract with NASA; the IRTF, which is operated by the University of Hawaii under Cooperative Agreement NNX-08AE38A with NASA, Science Mission Directorate, Planetary Astronomy Program. This publication uses observations obtained at IRTF through program numbers 2010B022, 2011A083, 2011B083, 2012A065, 2012B021, 2014A048, 2014B082, and 2015B043, as well as through engineering time in the 2012A and 2012B semesters. The authors recognize and acknowledge the very significant cultural role and reverence that the summit of Mauna Kea has always had within the indigenous Hawaiian community. We are most fortunate to have the opportunity to conduct observations from this mountain.

Facility: IRTF (CSHELL).

REFERENCES

Akeson, R. L., Chen, X., Ciardi, D., et al. 2013, PASP, 125, 989
Anglada-Escudé, G., Plavchan, P., Mills, S., et al. 2012, PASP, 124, 586
Arfken, G. B., Weber, H.-J., & Harris, F. E. 2012, Mathematical Methods for Physicists, A Comprehensive Guide (New York: Academic)
Arriagada, P. 2011, ApJ, 734, 70
Bailey, J. I. I., White, R. J., Blake, C. H., et al. 2012, ApJ, 749, 16
Bean, J. L., Seifahrt, A., Hartman, H., et al. 2010, ApJ, 713, 410
Bell, C. P. M., Mamajek, E. E., & Naylor, T. 2015a, MNRAS, 454, 593
Bell, C. P. M., Mamajek, E. E., & Naylor, T. 2015b, MNRAS, 454, 593
Blake, C. H., Charbonneau, D., & White, R. J. 2010, ApJ, 723, 684
Blake, C. H., & Shaw, M. M. 2011, PASP, 123, 1302
Bonfils, X., Delfosse, X., Udry, S., et al. 2013, A&A, 549, 109
Bottom, M., Muirhead, P. S., Johnson, J. A., & Blake, C. H. 2013, PASP, 125, 240
Browning, M. K., Basri, G., Marcy, G. W., West, A. A., & Zhang, J. 2010, AJ, 139, 504
Butler, R. P., Vogt, S. S., Marcy, G. W., et al. 2004, ApJ, 617, 580
Butler, R. P., Wright, J. T., Marcy, G. W., et al. 2006, ApJ, 646, 505
Campbell, B., Walker, G. A. H., & Yang, S. 1988, ApJ, 331, 902
Cochran, W. D., & Hatzes, A. P. 1994, Ap&SS, 212, 281
Cochran, W. D., Hatzes, A. P., Endl, M., et al. 2002, AJ, 124, 565
Correia, A. C. M., Couetdic, J., Laskar, J., et al. 2010, A&A, 511, A21
Crockett, C. J., Mahmud, N. I., Prato, L., et al. 2011, ApJ, 735, 78
Cutispoto, G., Pastori, L., Guerrero, A., et al. 2000, A&A, 364, 205
Davison, C. L., White, R. J., Henry, T. J., et al. 2015, AJ, 149, 106
Delfosse, X., Forveille, T., Mayor, M., et al. 1998a, A&A, 338, L67
Delfosse, X., Forveille, T., Perrier, C., & Mayor, M. 1998b, A&A, 331, 581
Delorme, P., Lagrange, A.-M., Chauvin, G., et al. 2012, A&A, 539, A72
Desort, M., Lagrange, A.-M., Galland, F., Udry, S., & Mayor, M. 2007, A&A, 473, 983
Dravins, D. 2008, A&A, 492, 199
Dumusque, X., Pepe, F., Lovis, C., et al. 2012, Natur, 491, 207
Duncan, D. K., Vaughan, A. H., Wilson, O. C., et al. 1991, ApJS, 76, 383
Eiroa, C., Marshall, J. P., Mora, A., et al. 2013, A&A, 555, A11
Elliott, P., Bayo, A., Melo, C. H. F., et al. 2014, A&A, 568, A26
Endl, M., Cochran, W. D., Kürster, M., et al. 2006, ApJ, 649, 436
Endl, M., Cochran, W. D., Tull, R. G., & MacQueen, P. J. 2003, AJ, 126, 3099
Evans, T. M., Ireland, M. J., Kraus, A. L., et al. 2012, ApJ, 744, 120
Fabricius, C., Høg, E., Makarov, V. V., et al. 2002, A&A, 384, 180

Feigelson, E. D., Lawson, W. A., Stark, M., Townsley, L., & Garmire, G. P. 2006, AJ, 131, 1730
Figueira, P., Marmier, M., Bonfils, X., et al. 2010, A&A, 513, L8
Gagné, J., Lafrenière, D., Doyon, R., Malo, L., & Artigau, É 2014, ApJ, 783, 121
Gaidos, E., Mann, A. W., Lépine, S., et al. 2014, MNRAS, 443, 2561
Gálvez, M. C., Montes, D., Fernández-Figueroa, M. J., & López-Santiago, J. 2006, Ap&SS, 304, 59
Gao, P., Plavchan, P., Gagné, J., et al. 2016, PASP, in press (arXiv:1603.05997)
Gizis, J. E., Reid, I. N., & Hawley, S. L. 2002, AJ, 123, 3356
Głębocki, R., & Gnaciński, P. 2005, in Proc. 13th Cambridge Workshop on Cool Stars, ed. F. Favata, G. A. J. Hussain, & B. Battrick (Noordwijk: ESA), 571
Gray, R. O., Corbally, C. J., Garrison, R. F., McFadden, M. T., & Robinson, P. E. 2003, AJ, 126, 2048
Greene, T. P., Tokunaga, A. T., Toomey, D. W., & Carr, J. B. 1993, Proc. SPIE, 1946, 313
Griffin, R. F. 2013, Obs, 133, 322
Hawley, S. L., Gizis, J. E., & Reid, N. I. 1997, AJ, 113, 1458
Henry, T. J., Jao, W.-C., Pewett, T., et al. 2014, in American Astronomical Society Meetings 224, 12026
Henry, T. J., Jao, W.-C., Subasavage, J. P., et al. 2006, AJ, 132, 2360
Hernán-Obispo, M., Gálvez-Ortiz, M. C., Anglada-Escude, G., et al. 2010, A&A, 512, A45
Hernán-Obispo, M., Tuomi, M., Gálvez-Ortiz, M. C., et al. 2015, A&A, 576, A66
Herrero, E., Ribas, I., Jordi, C., Guinan, E. F., & Engle, S. G. 2012, A&A, 537, 147
Hormuth, F., Brandner, W., Hippler, S., Janson, M., & Henning, T. 2007, A&A, 463, 707
Horne, K. 1986, PASP, 98, 609
Hosey, A. D., Henry, T. J., Jao, W.-C., et al. 2015, AJ, 150, 6
Houdebine, E. R. 2010, MNRAS, 407, 1657
Howard, A. W., Johnson, J. A., Marcy, G. W., et al. 2010a, ApJ, 721, 1467
Howard, A. W., Marcy, G. W., Fischer, D. A., et al. 2014, ApJ, 794, 51
Howard, A. W., Marcy, G. W., Johnson, J. A., et al. 2010b, Sci, 330, 653
Howard, A. W., Sanchis-Ojeda, R., Marcy, G. W., et al. 2013, Natur, 503, 381
Irwin, J., Berta, Z. K., Burke, C. J., et al. 2011, ApJ, 727, 56
Isaacson, H., & Fischer, D. 2010, ApJ, 725, 875
Jenkins, J. S., Ramsey, L. W., Jones, H. R. A., et al. 2009, ApJ, 704, 975
Jenkins, L. F. 1952, General Catalogue of Trigonometric Stellar Parallaxes (New Haven, CT: Yale University Observatory)
Kaltenegger, L., & Traub, W. A. 2009, ApJ, 698, 519
Kasper, M., Apai, D., Janson, M., & Brandner, W. 2007, A&A, 472, 321
Keenan, P. C., & McNeil, R. C. 1989, ApJS, 71, 245
Kipping, D. M. 2013, MNRAS, 434, L51
Koen, C., Kilkenny, D., van Wyk, F., & Marang, F. 2010, MNRAS, 403, 1949
Kürster, M., Hatzes, A. P., Cochran, W. D., et al. 1994, Msngr, 76, 51
Lafrenière, D., Doyon, R., Marois, C., et al. 2007, ApJ, 670, 1367
Leggett, S. K. 1992, ApJS, 82, 351
Lépine, S. 2005, AJ, 130, 1680
Lépine, S., & Bongiorno, B. 2007, AJ, 133, 889
Livingston, W., & Wallace, L. 1991, NSO Tech. Rep., 91-001
López-Santiago, J., Montes, D., Crespo-Chacón, I., & Fernández-Figueroa, M. J. 2006, ApJ, 643, 1160
López-Santiago, J., Montes, D., Gálvez-Ortiz, M. C., et al. 2010, A&A, 514, A97
Macintosh, B., Graham, J. R., Barman, T., et al. 2015, Sci, 350, 64
Maldonado, J., Martínez-Arnáiz, R. M., Eiroa, C., Montes, D., & Montesinos, B. 2010, A&A, 521, A12
Malo, L., Artigau, É., Doyon, R., et al. 2014, ApJ, 788, 81
Malo, L., Doyon, R., Lafrenière, D., et al. 2013, ApJ, 762, 88
Mamajek, E. E., & Hillenbrand, L. A. 2008, ApJ, 687, 1264
Marchwinski, R. C., Mahadevan, S., Robertson, P., Ramsey, L., & Harder, J. 2015, ApJ, 798, 63
Marcy, G. W., Butler, R. P., Fischer, D., et al. 2001, ApJ, 556, 296
Marcy, G. W., Butler, R. P., Vogt, S. S., Fischer, D., & Lissauer, J. J. 1998, ApJL, 505, L147
Marcy, G. W., & Chen, G. H. 1992, ApJ, 390, 550
Martín, E. L., Guenther, E., Zapatero Osorio, M. R., Bouy, H., & Wainscoat, R. 2006, ApJL, 644, L75
Mason, B. D., Wycoff, G. L., Hartkopf, W. I., Douglass, G. G., & Worley, C. E. 2001, AJ, 122, 3466
Massey, P., & Hanson, M. M. 2013, in Planets (Dordrecht: Springer), 35
Mayor, M., & Queloz, D. 1995, Natur, 378, 355
Mayor, M., & Udry, S. 2008, PhST, 130, 014010
McCarthy, K., & Wilhelm, R. J. 2014, AJ, 148, 70
Meschiari, S., Laughlin, G., Vogt, S. S., et al. 2011, ApJ, 727, 117
Meschiari, S., Wolf, A. S., Rivera, E., et al. 2009, PASP, 121, 1016
Meschiari, S., Wolf, A. S., Rivera, E., et al. 2012, Astrophysics Source Code Library, ascl:1210.018
Messina, S., Desidera, S., Turatto, M., Lanzafame, A. C., & Guinan, E. F. 2010, A&A, 520, A15
Messina, S., Muro Serrano, M., Artemenko, S., et al. 2015, Ap&SS, 360, 51
Middelkoop, F. 1982, A&A, 107, 31
Mohanty, S., & Basri, G. 2003, ApJ, 583, 451
Montet, B. T., Bowler, B. P., Shkolnik, E. L., et al. 2015, ApJ, 813, 11
Montet, B. T., Crepp, J. R., Johnson, J. A., Howard, A. W., & Marcy, G. W. 2014, ApJ, 781, 28
Morin, J., Donati, J. F., Petit, P., et al. 2010, MNRAS, 407, 2269
Nelder, J. A., & Mead, R. 1965, CompJ, 7, 308
Neves, V., Bonfils, X., Santos, N. C., et al. 2013, A&A, 551, A36
Newton, E. R., Charbonneau, D., Irwin, J., et al. 2014, AJ, 147, 20
Nidever, D. L., Marcy, G. W., Butler, R. P., Fischer, D. A., & Vogt, S. S. 2002, ApJS, 141, 503
Noyes, R. W., Weiss, N. O., & Vaughan, A. H. 1984, ApJ, 287, 769
Ochsenbein, F., Bauer, P., & Marcout, J. 2000, A&AS, 143, 23
Orlov, V. G., Voitsekhovich, V. V., & Guerrero, C. A. 2012, RMxAA, 48, 177
Pace, G. 2013, A&A, 551, L8
Pandey, J. C., Medhi, B. J., Sagar, R., & Pandey, A. K. 2009, MNRAS, 396, 1004
Paulson, D. B., & Yelda, S. 2005, A&A, 442, 1031
Paulson, D. B., & Yelda, S. 2006, PASP, 118, 706
Pecaut, M. J., & Mamajek, E. E. 2013, ApJS, 208, 9
Pepe, F., Cameron, A. C., Latham, D. W., et al. 2013, Natur, 503, 377
Plavchan, P., Latham, D., Gaudi, S., et al. 2015, arXiv:1503.01770
Plavchan, P. P., Anglada-Escude, G., White, R., et al. 2013, Proc. SPIE, 88641J, 88641
Poppenhaeger, K., Robrade, J., & Schmitt, J. H. M. M. 2010, A&A, 515, A98
Prato, L., Mace, G. N., Rice, E. L., et al. 2015, ApJ, 808, 12
Queloz, D., Henry, G. W., Sivan, J. P., et al. 2001, A&A, 379, 279
Quillen, A. C., & Thorndike, S. 2002, ApJL, 578, L149
Reid, I. N., Cruz, K. L., Allen, P., et al. 2004, AJ, 128, 463
Reid, I. N., & Hawley, S. L. 2005, New Light on Dark Stars Red Dwarfs (Berlin: Springer-Verlag)
Reid, I. N., Hawley, S. L., & Gizis, J. E. 1995, AJ, 110, 1838
Reiners, A., Bean, J. L., Huber, K. F., et al. 2010, ApJ, 710, 432
Reiners, A., Joshi, N., & Goldman, B. 2012, AJ, 143, 93
Reiners, A., & Mohanty, S. 2012, ApJ, 746, 43
Reiners, A., Shulyak, D., Anglada-Escude, G., et al. 2013, A&A, 552, A103
Rivera, E. J., Laughlin, G., Butler, R. P., et al. 2010, ApJ, 719, 890
Rivera, E. J., Lissauer, J. J., Butler, R. P., et al. 2005a, ApJ, 634, 625
Rivera, E. J., Lissauer, J. J., Butler, R. P., et al. 2005b, ApJ, 634, 625
Robertson, P., Mahadevan, S., Endl, M., & Roy, A. 2014, Sci, 345, 440
Salim, S., & Gould, A. 2003, ApJ, 582, 1011
Sanchis-Ojeda, R., Rappaport, S., Winn, J. N., et al. 2013, ApJ, 774, 54
Santos, N. C., Mayor, M., Naef, D., Queloz, D., & Udry, S. 2001, in IAU Symp. 202, Planetary Systems in the Universe: Observation, Formation and Evolution, ed. A. Penny (San Francisco, CA: ASP), 1377
Schlieder, J. E., Lépine, S., & Simon, M. 2010, AJ, 140, 119
Schmidt, S. J., Hawley, S. L., West, A. A., et al. 2015, AJ, 149, 158
Seifahrt, A., Käufl, H. U., Zängl, G., et al. 2010, A&A, 524, A11
Shkolnik, E., Liu, M. C., & Reid, I. N. 2009, ApJ, 699, 649
Shkolnik, E. L., Anglada-Escudé, G., Liu, M. C., et al. 2012, ApJ, 758, 56
Skrutskie, M. F., Cutri, R. M., Stiening, R., et al. 2006, AJ, 131, 1163
Song, I., Bessell, M. S., & Zuckerman, B. 2002, A&A, 385, 862
Stelzer, B., Marino, A., Micela, G., López-Santiago, J., & Liefke, C. 2013, MNRAS, 431, 2063
Tanner, A., White, R., Bailey, J., et al. 2012, ApJS, 203, 10
Tokunaga, A. T., Toomey, D. W., Carr, J., Hall, D. N. B., & Epps, H. W. 1990, in Proc. SPIE, 1235, 131
Torres, C. A. O., Quast, G. R., da Silva, L., et al. 2006, A&A, 460, 695
Torres, C. A. O., Quast, G. R., Melo, C. H. F., & Sterzik, M. F. 2008, in ASP Monograph Publications, Young Nearby Loose Associations, Vol. I, ed. B. Reipurth (San Francisco, CA: ASP), 757
Trifonov, T., Reffert, S., Zechmeister, M., et al. 2015, A&A, 582, A54
Tuomi, M., Jones, H. R. A., Barnes, J. R., Anglada-Escudé, G., & Jenkins, J. S. 2014, MNRAS, 441, 1545
Udry, S., Bonfils, X., Delfosse, X., et al. 2007, A&A, 469, L43
van Leeuwen, F. 2007, A&A, 474, 653
Vyssotsky, A. N. 1956, AJ, 61, 201

White, R. J., Gabor, J. M., & Hillenbrand, L. A. 2007, AJ, 133, 2524
Worley, C. E., & Douglass, G. G. 1997, A&AS, 125, 523
Zirker, J. B. 1968, SoPh, 3, 164
Zuckerman, B., Song, I., & Bessell, M. S. 2004, ApJL, 613, L65
Zuckerman, B., Song, I., Bessell, M. S., & Webb, R. A. 2001, ApJL, 562, L87
Zuckerman, B., Vican, L., Song, I., & Schneider, A. 2013, ApJ, 778, 5